HHS Public Access

Author manuscript

Cell Rep. Author manuscript; available in PMC 2026 June 15.

Published in final edited form as:

Cell Rep. 2026 May 26; 45(5): 117355. doi:10.1016/j.celrep.2026.117355.

Proximity labeling proteomics maps radial glial ciliary proteins across the developing telencephalon

Xiaoliang Liu[1,*], **Oscar T. Gutierrez**[1], **Sabyasachi Baboo**[2], **Eva Cai**[3], **Gurleen Kaur**[1], **Yazan Al-Issa**[1], **Jolene K. Diedrich**[2], **John R. Yates III**[2], **Xuecai Ge**[1,3,4,*]

[1]Department of Molecular and Cell Biology, University of California, Merced, Merced, CA 95340, USA

[2]Department of Integrative Structural & Computational Biology, The Scripps Research Institute, La Jolla, CA, USA

[3]Division of Biomedical Sciences, School of Medicine, University of California, Riverside, Riverside, CA 92521, USA

[4]Lead contact

SUMMARY

Primary cilia in radial glia act as signaling hubs essential for brain development, yet their molecular roles remain poorly understood. Here, using proximity-labeling-mediated *in vivo* proteomics, we systematically mapped ciliary proteins in the developing telencephalon. Our dataset reveals region-specific ciliary composition across the dorsal and ventral telencephalon. We identified and validated ribosome proteins and translational machinery components in radial glial cilia. Further, we uncovered ciliary roles for neurodevelopmental disorder-associated proteins, including MARCKS, a key regulator of radial glial polarity, and CKAP2L, a protein linked to Filippi syndrome. Functional studies show that MARCKS contributes to ciliogenesis and CKAP2L regulates neurogenesis by modulating Hedgehog signaling. These findings highlight previously unrecognized mechanisms by which primary cilia modulate brain formation. Our *in vivo* ciliary proteomic dataset provides a unique resource for understanding ciliary functions in brain development and developmental disorders.

Graphical abstract

*Correspondence: xuecaig@ucr.edu (X.G.), xiaoliang.liu01@hotmail.com (X.L.).

AUTHOR CONTRIBUTIONS

Conceptualization, X.G.; methodology, X.G., X.L., and S.B.; investigation, X.L., O.T.G, E.C., S.B., G.K., Y.A., and J.K.D.; writing – original draft, X.G. and X.L.; writing – review and editing, X.G., X.L., S.B., and J.R.Y.; fund acquisition, X.G. and J.R.Y.; supervision, X.G. and J.R.Y.

DECLARATION OF INTERESTS

The authors declare no competing interests.

DECLARATION OF GENERATIVE AI AND AI-ASSISTED TECHNOLOGIES IN THE WRITING PROCESS

The authors used ChatGPT, developed by OpenAI, for language editing assistance in this manuscript. ChatGPT was solely utilized for language proof-reading purposes and did not contribute to or influence any intellectual content within the manuscript.

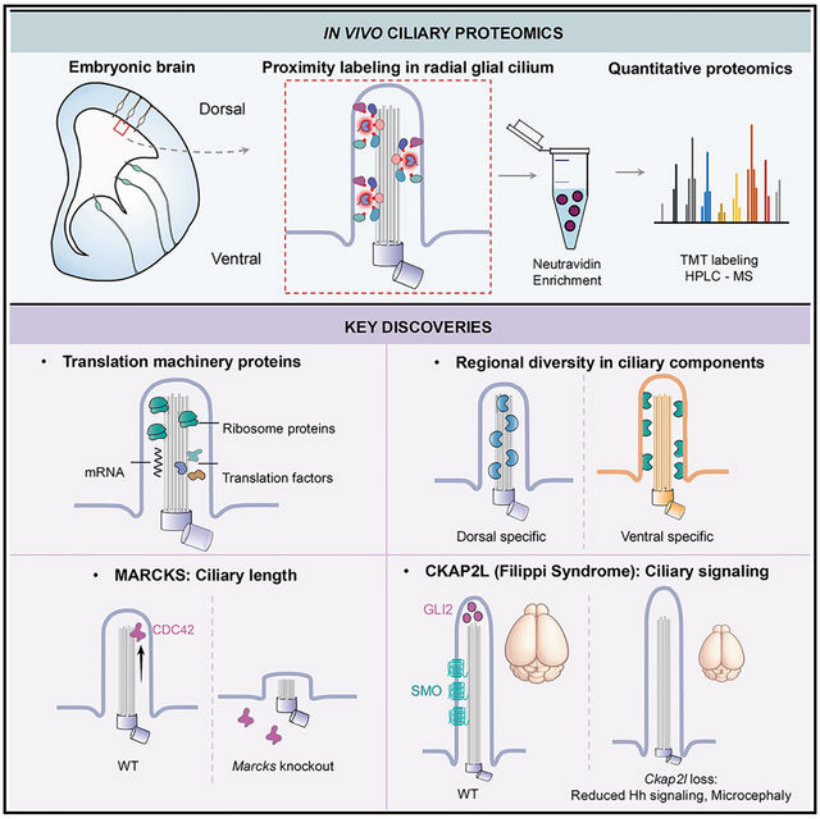

In brief

Primary cilia on neural progenitors serve as signaling hubs during brain development. Using *in vivo* proteomics, Liu et al. mapped ciliary proteins in the embryonic telencephalon, uncovering region-specific composition and the presence of ribosomes and translation machinery. Studies on neurodevelopmental disorder proteins MARCKS and CKAP2L highlight the ciliary mechanism during neurogenesis.

INTRODUCTION

The primary cilium is a microtubule-based sensory organelle projecting from the cell surface. Often referred to as the cell's antenna, the primary cilium senses a diverse array of signaling cues from the surrounding environment and transduces them into intracellular signaling pathways that elicit specific cellular responses.[1] Unique receptors and signaling transducers are concentrated in the primary cilia of different organs, enabling cells to respond to specific environmental cues.[2,3] Dysfunction of primary cilia leads to a wide range of diseases, collectively known as ciliopathies.[4] Brain structural abnormalities, such as microcephaly, neuronal heterotopia, disrupted cortical lamination, and cerebellar hypoplasia, are common features of ciliopathies.[5–10] These structural deficits typically arise from abnormal brain development during embryogenesis.[11] However, the precise roles of primary cilia in cortical formation remain underexplored.

The embryonic neurogenesis of the mammalian telencephalon begins with radial glia (RG), which produce most neurons in the cortex. Over the course of embryonic neurogenesis, RG strikes an intricate balance between self-renewal and neuronal production.[12] They first proliferate to expand the neural progenitor pool, followed by several rounds of neurogenic divisions to produce neurons. At the end of neurogenesis, the RG population is depleted as they differentiate into astrocytes, oligodendrocytes, or ependymal cells.[13,14] The mechanisms governing this balance are not fully understood. A crucial yet under-investigated area is the role of RG primary cilia, which serve as signaling hubs. The primary cilia of RG extend from the ventricular surface and are strategically positioned to detect regulatory molecular cues in their environment.[15–17] Understanding the specific protein components within the cilia of RG is essential for understanding their signaling roles, but comprehensive studies in this area are still lacking.

RG in the developing brain constitutes a highly heterogeneous population, displaying significant diversity across different brain regions.[18–22] The most well-established heterogeneity lies between the dorsal and ventral telencephalon, where RGs exhibit distinct molecular profiles and contribute differently to brain development. In the dorsal telencephalon (i.e., neocortex), RG expresses markers such as PAX6 and SOX2, and primarily generates excitatory projection neurons.[23] These neurons migrate radially to the cortical plate, forming cortical layers in an inside-out manner.[24] In contrast, in the ventral telencephalon (i.e., the lateral, medial, and caudal ganglionic eminences—LGE, MGE, and CGE), RG gives rise to inhibitory neurons.[25,26] These inhibitory neurons migrate tangentially into the dorsal cortex, where they integrate into circuits with the excitatory projection neurons.[27] This heterogeneity of RG is essential for the precise regulation of neurogenesis over space and time, enabling the establishment of complex neural circuits.[28–30] It remains unclear what signaling components are differentially enriched in the primary cilia of RG across these distinct telencephalic regions. This limits our understanding of whether region-specific ciliary signaling contributes to the divergent cell properties of RG in the dorsal and ventral telencephalic regions.

To unravel the roles of primary cilia during brain development, a critical step is to identify the bona fide protein components in the cilia of RG. A comprehensive map of genuine ciliary proteins in RG will provide critical insights into the mechanisms underlying RG specification and their spatial and temporal functions across the developing telencephalon. This is a challenging task because the primary cilium constitutes ~1/10,000 of the total cell volume; conventional approaches of physically isolating cilia usually contain contaminations from non-ciliary structures. In addition, some ciliary proteins are present in the cilium at very low abundance, and most signaling transducers transit through the cilia in a very dynamic manner. Physical isolation is not able to capture this dynamic protein presence in the cilium. Proximity labeling strategies have proven effective in identifying ciliary proteins in cultured cells.[31,32] In a previous study, we employed TurboID, an engineered biotin ligase, to profile ciliary proteins involved in Hedgehog (Hh) signaling.[33] This approach allowed us to capture low-abundant proteins in the cilia in response to Hh pathway activation.

Here, we leveraged TurboID-based proximity labeling to systematically map ciliary proteins in the RG of the mouse embryonic brain. We generated a Cilium-TurboID transgenic mouse model and performed quantitative ciliary proteomics in over 800 embryonic brains, providing both broad and deep coverage of the ciliary proteome during brain development. Our results revealed region-specific differences in ciliary composition between the dorsal and ventral cortex. Further, our dataset uncovered molecular machinery for local protein synthesis in the cilia of RG, suggesting an unexpected mechanism of ciliary regulation. Finally, our proteomic analysis identified a set of ciliary proteins linked to neurodevelopmental disorders (NDDs), leading to the discovery of previously unrecognized ciliary mechanisms underlying these conditions. Together, our dataset provides a unique resource for exploring the understudied biology of primary cilia in the developing brain and the molecular etiology of NDDs.

RESULTS

Construction of the mouse model for *in vivo* biotinylation of ciliary proteins in RG in the developing brain

To selectively label proteins in the primary cilia of RG, we generated a transgenic mouse line in which the transgene Cilium-TurboID is specifically targeted to the cilia, and its expression is driven by the brain lipid-binding protein (BLBP) promoter (Figure 1A). The transgenic mice were generated via the piggyBac transposon system.[34] In the transgene, TurboID is fused to a truncated form of ARL13B (ΔARL13B), which was created in our previous study and has been characterized to specifically localize to the cilium without disturbing ciliary morphology and function.[33] The BLBP promoter is active in RG from the early developmental stage (E10.5) throughout cortical development.[35,36]

The transgene has no discernible effect on the development or function of any organs, and the brain size and morphology are indistinguishable from those of wild-type (WT) mice (data not shown). In this transgenic mouse line, we first confirmed that Cilium-TurboID was expressed in RG within the embryonic brain. Immunofluorescence staining on coronal sections shows that the transgene is specifically expressed in all primary cilia of RG at the ventricular surface across both dorsal and ventral regions but not in the cilia of mature neurons in the cortical plate (Figures 1B and 1C). To validate the activity of TurboID in the cilium, we incubated the freshly dissected embryonic cortices in biotin and prepared whole-mount cortical tissues by exposing the inner ventricular surface. We then directly imaged the primary cilia from the *en face* perspective (Figure 1D). We found that all primary cilia at the ventricular surface of the transgenic mouse telencephalon were strongly labeled after a 15-min incubation with biotin (Figure 1E). Further, in the transgenic mouse brain without exogenous biotin, a low-level biotinylation signal in the cilia was detected, suggesting that TurboID can biotinylate ciliary proteins using the endogenous pool of biotin. In contrast, no biotin signal was detected in the cilia of WT brain.

To enrich biotinylated proteins from the mouse brain, we tested beads coated with either streptavidin or neutravidin. Both proteins bind biotin with extremely high affinity (Kd $\approx 10^{-14}$ to 10^{-15} M); however, compared to streptavidin, neutravidin exhibits lower non-specific binding due to its neutral charge and the absence of glycosylation and the RYD

sequence.[37–39] It is important to note that the recommended washing protocols for these beads differ, with streptavidin beads tolerating more stringent conditions. Indeed, we found that the overall protein intensities enriched by streptavidin beads are indistinguishable between WT and Cilium-TurboID brains. In contrast, with the same amount of total protein input, neutravidin beads enriched higher protein intensities from the Cilium-TurboID brains compared to the WT brains (Figures S1A and S1B). We hence used neutravidin beads to enrich biotinylated proteins in the subsequent proteomic assays.

In vivo ciliary proteomics in the developing mouse brain

Using the Cilium-TurboID transgenic mouse model, we sought to chart the profile of ciliary proteins in RG with quantitative proteomics in two brain regions: the dorsal (neocortex) and the ventral region (ganglionic eminences) telencephalon (Figure 2A). We focused on embryonic day 12.5 (E12.5), a critical stage when the RG population is abundant and actively balancing neurogenesis with self-amplification. For each labeling condition (WT + biotin, transgenic + biotin, and transgenic + vehicle), 420–430 embryonic brains were collected. An equal amount of 14 mg total protein input per condition was used, evenly divided into three replicates for enrichment with neutravidin beads (Figure S2A). The enriched proteins were digested on the beads and tagged with a 10plex tandem mass tag (TMT) label set. The multiplexed samples were then analyzed using HPLC-MS/MS for protein identification and quantification (Figure 2A).

For data analysis, we defined the relative protein abundance as the ratio of normalized abundance in each channel over the reference channel. The heatmap of each protein's relative abundance and the correlation of biological replicates demonstrated high reproducibility across the triplicates (Figures 2B and S2B). We then took the ratio of protein abundance in the TMT channel of the biotin-labeled transgenic brain over that in the biotin-labeled WT brain. The condition of transgenic + vehicle is not used due to its high "background" labeling by TurboID in the cilium (Figure S1D). Volcano plots were generated depicting statistical significance versus fold-change ratios (Figures 2C and 2D). Given the substantially reduced non-specific binding to neutravidin beads and the relatively smaller number of proteins identified, we applied a cut-off of fold-change ratio >1.2. We obtained 198 and 191 ciliary candidate proteins from the dorsal and ventral regions, respectively (Table S1). This filtering threshold allowed us to include low-abundance and moderately enriched candidates that have been reported as ciliary proteins in previous studies (blue dots in Figures 2C and 2D). In total, we identified 258 proteins as ciliary candidates after combining the dorsal and central telencephalon (Table S1, combined candidates D + V). Among them, 33 candidates have been previously reported to associate with cilia, including ciliary signaling regulators (INPP5E, PALD1, GSK3B, and IRS1), proteins involved in ciliary structure and ciliogenesis (tubulins, CFAP20, FLNA, and FLNB), and those associated with protein sorting and trafficking (TULP3, UNC119, PACS1, KIF5B, and RAN) (Figure S2C; Table S1, previously reported). Because candidates INPP5E, PALD1, CKAP2L, and DHX57 were not identified in any of the three replicates in WT samples, they had infinite $\log_2$(FC). We therefore listed these proteins separately and placed them next to the *y* axes (Figures 2C and 2D).

We performed statistical analysis on the mass spectrometry results and provided the list of statistically confident candidates in Table S1 (worksheet "candidates $p < 0.05$"; also represented in the upper right quadrant in volcano plots in Figures 2C and 2D). The corresponding false discovery rates (FDR, defined by q value[40]) is 14.6% for the dorsal telencephalon and 19.4% for the ventral telencephalon. Under this filtering threshold, we obtained 72 and 30 ciliary candidates from the dorsal and ventral regions, respectively.

We analyzed the 258 candidates that passed the fold-change >1.2 filter with Gene Ontology (GO) analysis. Enrichment analyses of biological processes, as well as KEGG and CORUM pathways, revealed that these 258 ciliary candidates participate in diverse pathways and biological processes (Figure 2E). In addition to expected terms such as cytoskeleton organization, intracellular transport, and pallium development, the top 20 enriched clusters include unexpected categories, such as protein translation regulation, RNA binding, and RNA localization. In the following studies, we sought to validate this dataset by confirming the ciliary localization of unexpected ciliary candidates and determining the ciliary functions of proteins previously linked to brain developmental disorders.

Embryonic brain ciliary proteomics uncover translation machinery components in the cilia of RG

Out of the 258 ciliary candidates in our dataset, 68 proteins (26%) belong to ribosome components and translation factors (Figure S3A). Notably, these proteins were also uncovered as ciliary candidates in a few previous proteomic studies in other systems, such as IMCD3 cells,[31,32,41,42] NIH3T3 cells,[33] and mouse brain ependymal cells[43] (Figures 3A and S3B; Table S2). Further, the study on ependymal cells demonstrated that local protein synthesis supports the structure and function of motile cilia.[43] Yet, ribosome components and translation factors have not been identified in primary cilia. This prompted us to validate the presence of such candidates in the primary cilium.

We performed immunofluorescence staining on whole-mount mouse cortical preparation and imaged primary cilia from the *en face* perspective (Figure S4A). The results demonstrate that multiple components of translation machinery are present in the cilia of RG, including ribosome components, RPS23 and RPL19, and translation factors, EIF3C, EEF2, and EEF1G (Figures 3B–3F and S4B–S4E). Certain ribosome components, such as RPL23A, specifically localize to the basal body (Figure S4F). Other ribosome components, such as RPS3, RPL11, and RPL10A, have previously been identified in the motile cilia of brain ependymal cells.[43] However, in RG cells, their high signal levels in the cell body precluded us from resolving individual cilia in the whole-mount cortices. Nevertheless, we validated their presence in the cilia of NIH3T3 cells (Figures S4H–S4J).

Next, we sought to detect the presence of mRNA in the cilia of RG. On the whole-mount mouse cortices, we conducted RNA fluorescence *in situ* hybridization (FISH) using a biotin-conjugated Oligo(dT) probe, which was subsequently detected with streptavidin-HRP followed by an HRP substrate reaction (Figure 3G). Simultaneously, we carried out immunofluorescence staining to label the cilia. Our results revealed a robust Oligo(dT) signal in the cilia of RG, suggesting the presence of polyadenylated mRNA (Figure 3H). Further, this signal was abolished by RNase A treatment, confirming its RNA specificity.

In contrast, when the FISH assay was performed in NIH3T3 cells, no poly(A) signal was detected in the cilium (Figures S4K and S4L).

Taken together, our results demonstrate the presence of mRNA and translation machinery in the cilia of RG in the embryonic cortex.

Identification of ciliary mechanisms for NDD-associated proteins

Ciliary dysfunction is widely implicated in NDDs.[5,6] To explore this connection, we compared our brain ciliary proteomic dataset with curated gene sets associated with NDDs, including Pre-birth BrainSpan, SynGO, and GeneTrek.[44] A total of 204 ciliary candidates in our dataset overlap with at least one of these resources, and 46 candidates overlap with all three (Figure 4A; Table S3). To gain further insights, we focused on the candidates in the 46 proteins that have well-established functions in brain development but have not yet been characterized as ciliary proteins. Among them, myristoylated alanine-rich C-kinase substrate (MARCKS) emerges as a top candidate.

MARCKS is a membrane-associated protein and a putative substrate of protein kinase C (PKC).[45,46] Loss of *Marcks* leads to severe neurodevelopmental defects, including failed neural tube closure, incomplete brain hemisphere separation, and disorganization of the RG scaffold.[47–50] The underlying molecular mechanisms remain poorly understood. To identify the role of MARCKS in the primary cilia, we first validated its ciliary localization. MARCKS-YFP localizes to the cilium when expressed in NIH3T3 cells. Further, immunostaining with a MARCKS antibody revealed its presence in the cilia in various cell types, including NIH 3T3, SH-SY5Y, and human RPE cells (Figures S5A and S5B). Immunostaining on whole-mount embryonic cortices shows that MARCKS is present in the primary cilia of RG across dorsal and ventral regions (Figure 4B).

Previous studies have shown that the membrane association of MARCKS is mediated by the myristoylation of its first glycine residue (G1).[51–53] In addition, PKC phosphorylation has been mapped to three serine residues (S152, S156, and S163) in its internal domain[54] (Figure 4C). Genetic studies showed that the myristoylation modification, but not PKC phosphorylation, is needed for MARCKS' role in radial glial scaffold organization.[49] To determine whether these post-translational modifications regulate the ciliary localization of MARCKS, we constructed mutants that abolish either myristoylation (G-A mutation) or phosphorylation (3S-3A mutation) and assessed their subcellular localization in NIH3T3 cells. We found that the myristoylation mutant completely lost its localization to the primary cilia, whereas the phosphorylation mutant retained ciliary localization similar to WT MARCKS (Figures 4D and 4E). Hence, MARCKS' ciliary localization depends on its myristoylation but does not require PKC phosphorylation.

To identify the functional role of MARCKS in the primary cilium, we generated *Marcks* knockout cells via CRISPR/Cas9 in NIH3T3 cells. Western blot results confirmed its depletion at the protein level (Figures S5C and S5D). *Marcks* knockout significantly reduced the ciliation rate. Moreover, in the remaining ciliated cells, the ciliary length was dramatically shortened compared to WT cells (Figures 4F–4H). To unravel the underlying mechanism of MARCKS in ciliogenesis, we focused on its previously reported role in

targeting cell polarity-related proteins, such as CDC42.[49] CDC42 facilitates vesicular trafficking essential for delivering components to the growing cilium,[55–57] and its levels in the cilium serve as an indicator of its activity during this process. To test it, we silenced *Marcks* expression with shRNA in a human RPE cell line, ARPE-19 (Figure S5E), in which ciliary CDC42 levels can be readily detected by antibody staining. We found that *Marcks* knockdown significantly reduced CDC42 levels in the cilium (Figures 4I and 4J). The cilium length in RPE cells is also significantly shortened by *Marcks* knockdown (Figure 4K).

Collectively, these data suggest that loss of *Marcks* blocks the targeting of CDC42 to ciliogenesis sites, thereby impairing the vesicular transport essential for cilium assembly. As a result, cells exhibit either absent or shortened cilia (Figure 4L). It is likely that the neurodevelopmental defects observed in *Marcks* knockout mice are partially linked to defective ciliogenesis and disrupted ciliary function in neural progenitors during brain development.

Brain cilium proteomics uncovers region-specific variations in ciliary composition of RG

Our cilium proteomic dataset indicates an intriguing difference in the protein compositions of cilia between the dorsal and ventral telencephalon (Figures 2B–2D, Table S1). Further analysis identified 67 proteins specifically enriched in the dorsal region, 60 in the ventral region, and 131 proteins common to both regions (Figure 5A, Table S4).

To further investigate region-specific ciliary localization, we validated the top candidates: cytoskeleton associated protein 2-like (CKAP2L) in the dorsal region, and DExH-box helicase 57 (DHX57) in the ventral region. Notably, cilium localization of these two proteins has not been previously reported. Immunostaining in NIH3T3 cells shows that both proteins are present in the cilium (Figure 5B). To determine their localization in the cilia of RG, we prepared immunofluorescence staining on whole-mount E12.5 cortices. We mounted the dorsal and ventral (LGE and MGE) telencephalon separately based on their relative positions and surface contours. We then imaged the cilia of RG at the inner ventricular surface from the *en face* perspective. We found that CKAP2L is present in the majority of cilia in the dorsal region (88.9% ± 3.3%), whereas only a small portion of cilia in the ventral region contain CKAP2L (31.6% ± 9.39%) (Figures 5C and 5D). In contrast, DHX57 is present in most cilia in the ventral region (56.9% ± 15.9%) and only a small fraction of cilia in the dorsal region (5.4% ± 4.1%) (Figures 5F and 5G). Intriguingly, western blot analysis reveals that the total expression levels of both proteins are comparable between the dorsal and ventral cortex (Figures 5E and 5H).

These results suggest that the region-specific ciliary localization is not due to variations in overall protein expression but rather reflects distinct regulatory mechanisms that govern protein targeting to cilia in different brain regions. In addition, the reciprocal ciliary localization patterns of CKAP2L and DHX57 validate our initial findings in the proteomic dataset, highlighting region-specific variations in ciliary composition between the dorsal and ventral brain regions.

CKAP2L regulates cilium-dependent cell signaling

Next, we characterized the roles of ciliary candidates identified from our proteomic dataset in cilium-dependent cell signaling, focusing on CKAP2L. Loss-of-function mutations in CKAP2L lead to Filippi syndrome, a rare genetic disorder characterized by short stature, microcephaly, intellectual disability, and syndactyly.[58–63] CKAP2L was originally identified as a mitotic spindle-associated protein in neural progenitors of both the embryonic and adult brain.[64] In addition to mitotic spindles in dividing cells (data not shown), we found that CKAP2L localizes to the primary cilia of interphase cells in multiple cell types, including RG (Figure 5C), NIH3T3 cells (Figure 5B), SH-SY5Y, and human RPE cells (Figure S6A). Expansion microscopy reveals that CKAP2L distributes along the ciliary axoneme, consistent with its known role as a microtubule-associated protein[65] (Figure S6B).

To determine the mechanistic roles of CKAP2L, we generated *Ckap2l* knockout (KO) NIH3T3 cells using CRISPR-Cas9 (Figure S6D). Western blot analysis with a validated CKAP2L antibody confirmed efficient depletion of CKAP2L proteins (Figures 6A and S6E). *Ckap2l* KO cells exhibit no abnormalities in cilium length or ciliation rate, and the chromosome segregation and cell cycle progression remain normal (data not shown). Next, we determined its role in ciliary signal transduction. The Hh pathway is the well-characterized cilium-dependent signaling, and the symptoms of Filippi syndrome patients resemble defects in Hh signaling.[58,66] Therefore, we assessed Hh signaling activity in *Ckap2l* KO cells after stimulation with the Sonic Hedgehog (Shh) ligand. qPCR analysis on two Hh pathway target genes, *Gli1* and *Ptch1*, showed that the Shh-induced transcript levels of both genes were markedly reduced in *Ckap2l* KO cells compared to those in WT cells (Figures 6B and 6C). These results suggest attenuated Hh signaling in *Ckap2l* KO cells.

The Hh signaling is transduced across the membrane by Smoothened (SMO), a GPCR-like receptor that is translocated and activated in the cilium. Active SMO then triggers a signaling cascade that eventually leads to the activation of transcription factor GLI2 at the ciliary tip.[67] To determine whether CKAP2L is required for this process, we assessed SMO and GLI2 ciliary levels in *Ckap2l* KO cells via immunofluorescence staining. We found that Shh-induced ciliary accumulation of both SMO and GLI2 is significantly reduced in *Ckap2l* KO cells compared to WT cells (Figures 6D–6G). Thus, CKAP2L positively regulates Hh signaling by facilitating SMO translocation to the cilium, which subsequently promotes GLI2 activation.

To exclude potential off-target effects of CRISPR/Cas9, we reintroduced the CKAP2L protein in *Ckap2l* KO cells via lentivirus-mediated gene expression. Unfortunately, CKAP2L-full length leads to disorganized mitotic spindles and distorted nuclei in a significant percentage of cells, as reported in a previous study[64] (Figure S6C), preventing the proper assessment of Hh signal activity. The CKAP2L protein features a CKAP2-superfamily domain at the C terminus and a more diversified N terminus (Figure 6H). Interestingly, we found that the N-terminal domain predominantly localizes to the primary cilium, whereas the C-terminal domain is exclusively present in the nucleus (Figures 6I and 6J). Further, expressing the C-terminal domain led to disorganized nuclei in nearly all infected cells. Finally, expressing the N-terminal domain in *Ckap2l* KO cells was sufficient to restore Shh-induced Hh signaling (Figure 6K). These results indicate that CKAP2L's

ciliary and nuclear functions are separable: the N terminus alone suffices to regulate Hh signaling in the cilium, while the C terminus acts in the nucleus.

Ckap2l loss disrupts brain development and Hh signaling in the developing cortex

To determine the roles of CKAP2L in brain development, we generated a genetic mouse model of *Ckap2l* knockout via CRISPR/Cas9 (Figures S7A and S7B). Western blot analysis on the cortices confirmed the complete removal of CKAP2L from the homozygous brain (Figure S7C). The *Ckap2l* KO mice (*Ckap2l*$^{-/-}$) are born at the expected Mendelian ratio. However, they appear runty, exhibit reduced body size, and most are unable to breed. The brain size in adult *Ckap2l* KO mice is reduced across multiple dimensions (Figures S8A–S8F). Sagittal sections of the brain at the same mediolateral level show that most brain regions are smaller in *Ckap2l* KO mice compared to WT mice, with pronounced underdevelopment in the cortex and most cerebellar lobules (Figure S8G).

As *Ckap2l* loss in NIH3T3 cells leads to reduced Hh signaling (Figure 6), we tested Hh signaling levels in the developing cortex. Among the three GLI transcription factors, GLI3 plays a predominant role in dorsal telencephalon development and is essential for balancing neural progenitor proliferation and differentiation.[68–70] Hh signaling is suppressed by GLI3R, a proteolytic product of GLI3 full length. Activation of the Hh pathway ceases the GLI3 proteolytic cleavage, reducing GLI3R production. The relative abundance of GLI3R often serves as an indicator of Hh signaling intensity. We therefore examined the GLI3R levels in the dorsal and ventral regions of WT and *Ckap2l*$^{-/-}$ telencephalons via western blot. We found a significant increase in Gli3R levels in the dorsal region of *Ckap2l*$^{-/-}$ mice compared to the WT mice (Figures S8H and S8I). However, the GLI3R levels in the ventral region were comparable between WT and *kap2l*$^{-/-}$ brains. This result aligns with diminished Hh signaling observed in *Ckap2l* KO NIH3T3 cells. Further, the dorsal-specific effect on Hh signaling corroborates our findings that CKAP2L is primarily localized to cilia in the dorsal but not the ventral telencephalon (Figure 5).

Ckap2l loss reduces embryonic neurogenesis in the developing brain

In the developing telencephalon, Hh signaling is essential for maintaining the neural progenitor pool in the dorsal cortex, and its reduction leads to decreased cortical size.[71,72] Therefore, we examined neural progenitor populations in the developing cortex using immunostaining for SOX2, a marker of RG, and TBR2, a marker of intermediate neural progenitors (INPs). In E13.5 *Ckap2l*$^{-/-}$ mice, both SOX2-positive and TBR2-positive layers were significantly thinner compared to WT mice. In addition, the overall thickness of the cerebral cortex was reduced in *Ckap2l*$^{-/-}$ embryos relative to WT controls (Figures 7A and 7B). Thus, *Ckap2l* loss reduces the neural progenitor pool in the developing dorsal cortex.

Next, we determined the impact of *Ckap2l* loss on neurogenesis. By E16.5, when early born CTIP2-positive neurons are generated, we found a reduced population of CTIP2-positive neurons in *Ckap2l*$^{-/-}$ embryos compared to WT littermates (Figures 6C and 6D). This reduction is not due to developmental delay, as the CTIP2-positive neuronal layer remains thinner in *Ckap2l*$^{-/-}$ cortices at postnatal stages (P3 and P7). Furthermore, the layer of later-born CUX1-positive neurons is also thinner in the *Ckap2l*$^{-/-}$ brain compared to the WT

littermates (Figures 7E, 7F, S9A, and S9B). Finally, this reduction in neuronal populations is consistently observed across the entire rostral-caudal axis (Figures S9C and S9D). In addition, CKAP2L loss also reduced the neural progenitor pool in the anterior subventricular zone and the granule cell layer (GCL) of the dentate gyrus in the newborn mouse brain (Figures S9E and S9F). Overall, these results suggest that *Ckap2l* loss reduced neural progenitor pools, leading to diminished neuronal production across all developmental stages, which ultimately results in reduced cortical size.

Shh functions as a critical mitogen for granule neuron precursors (GNPs) in the developing cerebellum.[73–75] Given that CKAP2L positively regulates Hh signaling, we next assessed GNP proliferation in the developing cerebellum. Immunostaining with the mitotic marker phospho-histone H3 (pH3) revealed a reduced number of proliferating cells in the external granule layer (EGL) of *Ckap2l*$^{-/-}$ cerebella compared to WT littermates (Figures 7G and 7H). Differentiated granule neurons migrate from the EGL to the internal granule layer (IGL); we further examined cerebellar architecture and found that both the IGL area and the total cerebellar area were significantly reduced in *Ckap2l*$^{-/-}$ cerebella compared to the WT littermates (Figures 7I and 7J). Thus, loss of *Ckap2l* reduced GNP proliferation, leading to cerebellar hypoplasia.

While the *Ckap2l* KO mouse model exhibits key features of Filippi syndrome, such as short stature and microcephaly, it fails to fully recapitulate other symptoms, such as syndactyly. Potential functional redundancy could be provided by other similar proteins, such as CKAP2, a paralog of CKAP2L. The two proteins share 16% amino acid identity and a C-terminal CKAP2 super-family domain.[76,77] We found that CKAP2 localizes to the primary cilia of multiple cell types, including NIH3T3, SH-SY5Y, and radial glial cells (Figures S10A and S10B). Whole-mount cortical staining further confirmed CKAP2's presence in the cilia of both the dorsal and ventral cortex (Figures S10C and S10D). To elucidate CKAP2's function, we used shRNA-mediated knockdown in NIH3T3 cells. While CKAP2 depletion did not affect ciliogenesis or ciliary length (Figures S10E–S10G), it significantly attenuated Shh-induced Hh pathway activation, as indicated by reduced *Gli1* transcript level (Figure S10H). Thus, CKAP2 acts as a positive regulator of Hh signaling and may functionally compensate for CKAP2L loss in certain contexts.

DISCUSSION

Brain structural deficits are common in ciliopathies, underscoring the critical roles of primary cilia in brain development.[5–10] Primary cilia are present in various cell types in the developing brain, including migrating newborn neurons, mature neurons, and neural progenitors. Ciliary defects likely disrupt key biological processes across all these cell types. In this study, we focused on cilia in RG and defined their *bona fide* ciliary protein composition using TurboID-mediated proximity labeling and quantitative proteomics. A number of previous studies using proximity labeling enzymes, such as BioID/BioID2, APEX/APEX2, and TurboID, have markedly expanded the repertoire of ciliary proteins.[31,42,78,79] However, it is important to note that these studies were conducted in cultured cell lines. The *in vitro* systems lack the multicellular interactions between diverse cell types and the dynamic signaling cues, such as morphogen gradients and fluid flow,

that shape ciliary function and protein composition *in vivo*. Therefore, *in vivo* studies are essential for accurately capturing the physiological complexity of the ciliary proteome in brain development. Indeed, beyond known ciliary proteins (Figure S2C), we identified a cohort of previously unrecognized ciliary candidates and uncovered the mechanistic roles of several in ciliary signaling and brain development. Our study represents a comprehensive dataset of the brain ciliary proteome and establishes a valuable resource for understanding cilium-mediated cell signaling in RG and the molecular basis of ciliopathies and brain developmental disorders.

Intriguingly, our study revealed region-specific variation in the ciliary composition of RG between the dorsal and ventral telencephalon. We validated this regional specificity by confirming CKAP2L ciliary localization in the dorsal region and DHX57 in the ventral region (Figure 5). While primary cilia across different cell types share core structural components, their functional protein composition can vary significantly depending on cell types and contexts. For instance, PDGFRA localizes to cilia in fibroblasts but not in RG.[33,80,81] Similarly, neuronal cilia may express unique receptors, such as NPY2R, which is absent in epithelial cells.[82,83] And SMO is detectable in the cilium only upon activation of Hh signaling.[83,84] Many factors could contribute to the differential ciliary localization, such as cell-type-specific gene expression, post-translational modifications, variations in ciliary trafficking machinery, and differential exposure to external signaling pathways. It is well-established that RG in the dorsal and ventral cortex represents distinct cell populations,[18–22] and they may also be exposed to different external signaling cues. Understanding the mechanisms that drive differential ciliary targeting in distinct RG subtypes and their functional implications highlights important directions for future study.

Our *in vivo* ciliary proteomics identified a set of translation machinery components, including ribosomal subunits and eukaryotic initiation and elongation factors (EIFs and EEFs) (Figures 3, S3, and S4). While many of these components have been detected in previous ciliary proteomes, none have been validated in the primary cilia.[33,41,85] Here, we provide direct evidence for the presence of translation machinery, as well as mRNAs, in the primary cilia (Figure 3). These findings support the potential presence of local protein synthesis in primary cilia. This concept appears to challenge the prevailing view that the intraflagellar transport (IFT) machinery is primarily responsible for delivering proteins to the cilium for assembly and maintenance.[86] Nevertheless, several notions suggest that local translation within cilia could be necessary under specific conditions.

First, local translation has been demonstrated in the motile cilia of brain ependymal cells, where it is essential for maintaining the proper ciliary function.[43] This finding supports the feasibility of protein synthesis within the ciliary microenvironment. Second, one of the translation factors validated in our study, EIF3, has been reported to directly regulate Hh signaling. Loss-of-function mutations in *Eif3* cause the *extra-toes spotting* (*Xs*) in mice, which is characterized by polydactyly—a hallmark of excessive Hh pathway activation.[87] Intriguingly, *Xs* mutants show no global translation defects but exhibit specific protein reduction in PTCH1, a key negative regulator of Hh signaling.[87,88] Further study revealed that EIF3C binds to a pyrimidine-rich motif in the 5′ UTRs of some transcripts, including *PTCH1*.[88] Together, the evidence suggests the possibility that EIF3C may be involved in

mRNA binding or translational regulation in the cilium. Finally, local translation is best established in neuronal growth cones and synapses, structures that are distal to the cell body and require on-site protein synthesis for rapid, spatially restricted responses.[89–92] Notably, RGs exhibit similar spatial features: their primary cilia remain anchored at the apical surface while the nucleus undergoes interkinetic nuclear migration (INM), oscillating between the apical and basal boundary of the ventricular zone in coordination with the cell cycle.[93,94] As a result, the cilium and nucleus are often separated over a long distance. Local translation in the cilia of RG may enable direct synthesis of structural or signaling proteins to ensure its structural integrity and timely responses to extracellular cues. It is important to note that our proteomic data indicate the presence of the translation machinery components in primary cilia; however, whether active protein translation occurs within the RG primary cilia, and what its functional significance might be, will require rigorous studies in the future. It is likely that local translation may not be a universal feature of primary cilia but instead represents a specialized adaptation in certain cell types, such as RG and brain ependymal cells,[43] to fulfill their specific functional requirements.

Our *in vivo* ciliary proteomics offered insights into the molecular underpinnings of NDDs. For example, we uncovered a ciliary role for MARCKS, a protein whose critical functions in embryonic mouse brain development were identified decades ago, yet its molecular mechanisms remain poorly understood.[47–50] Although MARCKS is a well-defined PKC substrate with conserved phosphorylation sites, genetic studies have shown that these sites are dispensable for brain development. Instead, its N-terminal myristoylation is essential.[49,51–54] Intriguingly, we found that the myristoylation site, but not the PKC phosphorylation sites, is required for MARCKS ciliary localization. These findings suggest that the ciliary function of MARCKS is fundamental during brain development. Furthermore, MARCKS plays a key role in ciliogenesis by recruiting CDC42 and facilitating CDC42-associated vesicle transport to support cilium formation (Figures 4F–4L). Remarkably, our results are consistent with the reported phenotype in zebrafish, where *Marcks* knockdown led to a significant reduction in cilium formation and ciliary length in Kupffer's vesicle of the zebrafish embryos.[95] To further contextualize this role, it is important to note that radial glial cells maintain a specialized apical membrane domain enriched with essential proteins, including the Par polarity complex (PAR6, PAR3, and aPKCζ) and CDC42.[49] Primary cilia extend from this apical domain, and both structures are essential for establishing a polarized radial glial scaffold. Disruption of these structures results in severe polarity defects in RG and brain developmental abnormalities characteristic of ciliopathies.[96,97] Therefore, the neurodevelopmental defects in *Marcks* mutants may result from impaired ciliogenesis and subsequent disruptions of ciliary signaling. However, it is also important to note that the effector domain of MARCKS exhibits strong affinity for binding calcium-calmodulin (CaM), filamentous actin (F-actin), and phosphatidylinositol 4,5-bisphosphate (PIP2). Upon phosphorylation by PKC, MARCKS translocates from the membrane to the cytosol. This redistribution modulates the actin cytoskeletal dynamics and vesicular trafficking,[98–101] thereby regulating key cellular processes such as changes in cell shape and the formation of cellular protrusions. These events are critical for proper neuronal migration, axon guidance, and neuritogenesis during brain development.[101–105] For future

studies, it will be intriguing to determine further how ciliary and non-ciliary MARCKS are integrated together to contribute to cortical development.

CKAP2L is another previously uncharacterized ciliary protein implicated in NDDs. Loss-of-function mutations in CKAP2L lead to Filippi syndrome. We thoroughly characterized the cilium localization of CKAP2L and pinpointed its N terminus as the ciliary targeting domain and the previously described nuclear localization domain to the C terminus. Consistent with previous studies, we found that overexpression of CKAP2L, particularly the C terminus, disrupted nuclear morphology by interfering with mitotic spindle assembly and chromosome segregation (Figures 6I and S6C).[64] Unlike previous reports, we found that CKAP2L loss-of-function does not disrupt chromosome segregation; instead, it impaired Hh signal transduction by restricting the ciliary translocation of SMO and subsequent GLI2 activation (Figures 6D–6G). Importantly, CKAP2L is present in nearly all cilia in the dorsal cortex but only in a subset in the ventral cortex. While the underlying mechanism requires future inquiry, this cell-type-specific cilium localization may explain the moderate phenotype in *Ckap2l* KO mice. Hh signaling functions as a morphogen that specifies ventral cell fates in the neural tube, and its reduction leads to dorsalization.[106] Surprisingly, *Ckap2l* KO mice show no obvious neural patterning defects, likely because CKAP2L is largely absent from ventral cilia, sparing Hh signaling in this region. However, after neural patterning, dorsal Hh signaling is critical to maintain RG and INP neural progenitor pools.[71,72] Consequently, *Ckap2l* loss disrupts neuronal populations in both the outer and inner cortical plates. Notably, *Ckap2l* KO mice do not recapitulate the syndactyly observed in human Filippi syndrome patients. While such mouse-human discrepancies are common, functional compensation by its paralog, CKAP2, may explain this difference. Like CKAP2L, CKAP2 localizes to primary cilia and promotes Hh signaling (Figure S10), potentially buffering the loss of CKAP2L in mice.

In this study, we used an intracellular TurboID-based strategy to capture both transmembrane proteins and downstream signaling components that define the cilium as a signaling hub. For the future, an approach with extracellular-facing proximity labeling enzymes (e.g., HRP or APEX2) to profile the ciliary surfaceome (surface-exposed proteins) will provide a complementary perspective of ciliary function. Here, our *in vivo* proteomic study offers a unique dataset of *bona fide* ciliary proteins in the developing mammalian brain. We identified previously uncharacterized ciliary proteins, expanding our understanding of the molecular landscape of primary cilia in neurodevelopment. Future studies leveraging this resource could further elucidate cilium-mediated signaling mechanisms and their roles in neurodevelopmental pathologies.

Limitations of the study

The expression level of the ΔArl13b-GFP-TurboID transgene in the developing brain is lower than that of endogenous Arl13b. While this low level of expression minimizes potential interference with normal embryonic development, it may limit biotinylation efficiency within the cilium. As a result, our proteomic dataset may underrepresent proteins that are present at low abundance in the cilium. In addition, we used neutravidin, rather than streptavidin, to minimize background binding to magnetic beads and thereby reduce

non-specific protein detection in mass spectrometry. This strategy improves specificity but reduces overall protein recovery. Subsequently, for data analysis, we favored fold-change as the primary filtering criterion to avoid excluding bona fide ciliary candidates. However, to facilitate broader use of the dataset by the research community, we also provide a list of statistically confident candidates ($p < 0.05$) in Table S1.

RESOURCE AVAILABILITY

Lead contact

Requests for further information and resources should be directed to and will be fulfilled by the lead contact, Xuecai Ge (xuecaig@ucr.edu).

Materials availability

All unique reagents generated in this study are available from the lead contact.

Data and code availability

- The mass spectrometry data have been uploaded to MassIVE using the identifier MSV000097579. The dataset can be downloaded from the MassIVE FTP server with this URL: ftp://MSV000097579@massive-ftp.ucsd.edu. This dataset can also be accessed in ProteomeXchange via PXD062788. All remaining data supporting the findings of this study are available within the paper and its supplemental information.
- This paper does not report original code.

STAR★METHODS

EXPERIMENTAL MODEL AND STUDY PARTICIPANT DETAILS

Mice: All mouse work was performed according to guidelines approved by the IACUC of the University of California, Merced (animal protocol no. 2023–1151) and University of California, Riverside (animal protocol no. 30906). All mice were maintained in a specific pathogen-free animal facility. Mice were monitored daily and housed in a 12 h light/12 h dark cycle, under the temperature of 66–72°F with 40–60% humidity. The *BLBP*-driven detlaARL13B-GFP-TurboID transgenic mice were generated in C57BL/6 mice by a PiggyBac strategy. Genotyping was performed using quantitative real-time PCR with primers detailed in key resources table. *Ckap2l*$^{-/-}$ mice were generated in C57BL/6 mice using CRISPR/Cas9, as described in Figure S7. Genotyping was performed using PCR with primers detailed in key resources table. Embryos were analyzed at the indicated stage described in the figure legends. Adult mice were euthanized by CO_2 inhalation followed by cervical dislocation. The sex has not been reported to affect primary cilium in the developing brain, and embryos of both sexes were studied without separating one from the other.

Cell lines: NIH3T3 cells (Cat#: CRL-1658), HEK293T cells (Cat#: CRL-3216), SH-SY5Y cells (Cat#: CRL-2266) and ARPE-19 cells (Cat#: CRL-2302) were purchased from ATCC and authenticated by the vendor. NIH3T3 cells were cultured in DMEM supplemented with 10% v/v calf serum, and ciliation was induced by reducing the growth media to 0.5% v/v

calf serum for 24 h. HEK293T cells were cultured in DMEM supplemented with 10% v/v fetal bovine serum. SH-SY5Y cells were cultured in DMEM/F12 medium supplemented with 10% v/v fetal bovine serum, and ciliation was induced by reducing the growth media to 0.25% v/v fetal bovine serum for 24–36 h. ARPE-19 cells were cultured in DMEM/F12 medium supplemented with 10% v/v fetal bovine serum, and ciliation was induced by DMEM/F12 medium without fetal bovine serum for 48 h. The HEK293T EcR-Shh-N cell line is a gift from Dr. Rajat Rohatgi lab, Stanford University. To induce Shh signaling, growth media were added with ShhN conditioned medium (20–30% v/v, optimal dilution varies batch-wise) produced from HEK293T EcR-Shh-N cells. Every cell line is routinely tested for mycoplasma contamination and confirmed negative before experiments.

METHOD DETAILS

Primary culture of radial glia cells: RG were isolated from cortexes of E12.5 embryos. Briefly, isolated cortexes were cut into small pieces and treated with Papain/DNase I. After trituration, single-cell suspensions were harvested by centrifugation and then resuspended in plating medium (Neurobasal medium supplemented with N2, Glutamax, penicillin/streptomycin and 10% Horse serum) for 4–6hr until cells adhered to the bottom of the culture dish. Then, the plating medium was changed into the culture medium (Neurobasal medium supplemented with N2, Glutamax, penicillin/streptomycin, and bFGF).

Generation of *Marcks* knockout NIH3T3 cells: *Marcks*$^{-/-}$ NIH3T3 cells were generated using CRISPR/Cas9-mediated genome editing with two guide RNAs: #1 (5′-AGGGAGAAGCCACCGCCGAG-3′) and #2 (5′-ATTTGCTTTGGAAGGCGACG-3′). The guide RNAs were selected according to the online tool Benchling (https://benchling.com/editor), and their sequences were cloned into the PX330-GFP plasmid, respectively. Cell line clones were obtained by single-cell sorting, and *Marcks* deletions were confirmed by immunofluorescence (IF) and Western blot with anti-MARCKS antibodies. Two independent CRISPR/Cas9 knockout cell clones were chosen for the analysis.

Generation of *Ckap2l* knockout NIH3T3 cells: *Ckap2l*$^{-/-}$ NIH3T3 cells were generated using the same method as generating *Marcks* knockout NIH3T3 cells. The two guide RNAs are #1 (5’ -GTCGCCGTAGAGCCATGGTG- 3′) and #2 (5′-CCGCGGCTGCGCTGGCAGTG- 3′).

TurboID labeling experiments and subcellular fractionation: TurboID labeling experiments were performed as described previously.[33] Briefly, the freshly dissected neocortex (dorsal telencephalon) and ganglion eminences (ventral telencephalon) were incubated in the Neurobasal medium in the presence of 50 μM biotin for 15 min. For non-labelled brain tissues, water was added instead of biotin. After 15 min of incubation at 37°C, the medium was removed quickly, and tissues were washed four times with 1× PBS and kept on ice. For immunofluorescence microscopy, tissues were immediately fixed in 4% PFA in PBS. For western blot and proteomic analysis, brain tissues were lysed by subcellular fractionation buffer (20 mM HEPES, 10 mM KCI, 2 mM $MgCl_2$, 1 mM EDTA, 1 mM EGTA, 1 mM DTT, pH 7.5 and protease inhibitors) and passed through a 27-G needle

15 times. Nuclei and mitochondria were separated from the supernatant by two sequential centrifugations at 3,000 rpm (720 × g) and 8,000 rpm (10,000 × g). The supernatant was then lysed in lysis buffer (0.5% NP-40, 0.1% SDS, 0.5% sodium deoxycholate, 150 mM NaCl, 50 mM Triethylammonium bicarbonate (TEAB), pH 7.5, and protease inhibitors), sonicated and finally clarified by centrifugation.

Enrichment of biotinylated proteins: For neutravidin capture, the lysates from the TurboID labeling experiments were measured to determine the protein concentrations and were then adjusted to equal concentrations and volumes as starting material. The lysates were added to washed and equilibrated neutravidin agarose resins, and biotinylated proteins were allowed to bind for 1.5 h at room temperature. Neutravidin agarose resins with bound proteins were washed 2 times with lysis buffer and 4 times with 1 × PBS. For Western blot analysis, the beads were eluted with 2 × SDS sample buffer.

Streptavidin capture was performed as described previously.[33] Briefly, the lysates were added onto washed and equilibrated streptavidin magnetic beads, and biotinylated proteins were then allowed to bind for 1.5 h at room temperature. Streptavidin beads with bound proteins were washed extensively with a series of buffers: 2 times with lysis buffer, 1 time with 1 M KCl, 1 time with 0.1 M Na_2CO_3, 1 time with 2 M Urea in 10 mM Tris-HCl, pH 8.0, 2 times with lysis buffer, and finally 2 times with 1 × PBS. For Western blot analysis, the beads were eluted with 2 × SDS sample buffer.

On-beads trypsin digestion and TMT labeling: Enriched proteins bound to beads were denatured with 8 M urea in 100 mM TEAB, disulfide bonds reduced with 5 mM TCEP and free cysteines alkylated with 2-Chloroacetamide. Denatured proteins bound to beads were precipitated with methanol-chloroform and digested with trypsin in 1 M urea and 100 mM TEAB. Resulting peptides were dried by vacuum centrifugation and then labeled with 10-plex TMT as described in the manufacturer's protocol. A reference TMT channel was used for internal normalization using a tenth of all protein in other 9 channels. TMT-labeled peptides were pooled, dried and reverse-phase fractionated into 4 parts at high pH using 12.5%, 17.5%, 22.5% and 50% acetonitrile, as per manufacturer's protocol.

Mass spectrometry: The samples were analyzed on a Fusion Lumos mass spectrometer. Samples were injected directly onto a 25 cm, 100 μm ID column packed with BEH 1.7 μm C18 resin. Samples were separated at a flow rate of 300 nL/min on a nLC 1200. Buffer A and B were 0.1% formic acid in 5% and 80% acetonitrile, respectively. A gradient of 1–25% B over 100 min, an increase to 40% B over 20 min, an increase to 90% B over another 10 min and held at 90% B for a final 10 min of washing was used for 140 min total run time. Column was re-equilibrated with 15 μL of buffer A prior to the injection of sample. Peptides were eluted directly from the tip of the column and nanosprayed directly into the mass spectrometer by application of 2.8 kV voltage at the back of the column. The Lumos was operated in a data dependent mode. Full MS1 scans were collected in the Orbitrap at 120k resolution. The cycle time was set to 3 s, and within this 3 s the most abundant ions per scan were selected for CID MS/MS in the ion trap. MS3 analysis with multinotch isolation (SPS3) was utilized for detection of TMT reporter ions at 7.5k resolution. Monoisotopic

precursor selection was enabled and dynamic exclusion was used with exclusion duration of 10 s.

MS data processing and analysis: Protein and peptide identification was done with Integrated Proteomics Pipeline (IP2, Bruker Scientific LLC). Tandem mass spectra were extracted from raw files using RawConverter,[107] and searched with ProLuCID[108] against a database comprising UniProt reviewed (Swiss-Prot) proteome for *Mus musculus* (UP000000589) with modified Arl13b (UniProt, Q640N2; amino acids 1 and 19–356 deleted, EGFP-TurboID fused at C terminus), Streptavidin (UniProt, P22629) added, and a list of general protein contaminants. The search space included semitryptic peptide specificity with unlimited missed cleavages. Carbamidomethylation (+57.02146 C) and TMT (+229.1629 K and N terminus) were considered static modifications. Data was searched with 50 ppm precursor ion tolerance and 500 ppm fragment ion tolerance. Identified proteins were filtered using DTASelect2[109] and utilizing a target-decoy database search strategy[110] to limit the false discovery rate to 1%, at the spectrum level. A minimum of one peptide per protein and one tryptic end per peptide were required, and precursor delta mass cutoff was fixed at 5 ppm. Statistical model for tryptic peptides (trypstat) was applied. Census2 isobaric-labeling analysis was performed based on the TMT reporter ion intensity using default parameters, thresholding isobaric purity at 0.6 and normalizing to the internal reference channel.[111]

Statistical analysis of mass spectrometry data: The raw data of peak intensities from mass spectrometry are provided in Table S1, worksheets “PeakIntensity_Dorsal” and “PeakIntensity_Ventral”. For data analysis, we calculated three values of fold-change ratio for each protein by dividing the mass spectrometry intensity in Tg+B samples by that in WT + B samples for each replicate. The three values of fold-change were used to compute the standard deviation (SD) and the standard error of the mean (SEM). After that, we calculated the absolute t-statistic as $t = |(\text{mean fold change} - 1)|/\text{SEM}$, where 1 represents no change between conditions. The p-value was calculated as the two-tailed probability from the Student’s t-distribution based on the calculated t-statistic and degrees of freedom. To account for multiple hypothesis testing, Benjamini–Hochberg adjusted p-values and q-values were subsequently computed.

As some candidates were not detected in one or more replicates of TMT channels, we calculated an aggregate ratio. For each candidate, the aggregate ratio was defined as the sum of mass spectrometry intensities across all three Tg+B replicates divided by the corresponding sum across WT + B replicates: $\sum(\text{Tg+B})/\sum(\text{WT + B})$. This allowed us to compute the fold-change ratios of all candidates excepts four - INPP5E, PALD1, CKAP2L, DHX57. These four proteins are our highest-confidence candidates and were listed separately in Figures 2C and 2D.

The results of the above statistical analysis are provided in Table S1, worksheet “AnalysisDorsal_Tg+B_vd_WT” and “AnalysisVentral_Tg+B_vd_WT”.

Candidates passing the filter of fold-change >1.2 are listed in Table S1 (worksheet “Candidates FC > 1.2). Candidates passing the filter of $p < 0.05$ are listed in Table

S1 (worksheet “Candidates $p < 0.05$). Mitochondrial proteins and histone proteins were excluded from these lists due to their known high levels of endogenous biotinylation and overall abundance.

GO analysis: Gene ontology (GO) enrichment analysis of biological processes was plotted according to the rich factor in Metascape (https://metascape.org/gp/#/main/step1). The top 20 enriched biological processes are represented in the scatterplot.

Whole-mount dissection and immunofluorescence: The E12.5 brains were harvested and fixed in 4% (w/v) paraformaldehyde (PFA) in 1x PBS for 2–12 h at 4°C. The brains were then rinsed 2 times with PBS and further dissected into dorsal and ventral regions. Prior to staining, the brain tissues were permeabilized with 0.2% Triton X-100 in PBS for 10min and blocked for 1 h in blocking buffer: 2% donkey serum in PBS. The brain tissues were incubated with primary antibody overnight at 4°C, washed 3 times with PBS and incubated with secondary antibody for 1h, followed by DAPI staining for 10 min at room temperature. The brain tissues were then dissected into small pieces before mounting with Fluoromount-G.

Cryostat sectioning and immunofluorescence: The dissected brains were fixed in 4% PFA in PBS overnight at 4°C and then incubated in 30% sucrose overnight or until they sunk to the bottom. The brains were embedded in O.C.T. compound and sliced into 10–20μm thick sections with Leica CM1850-3-1 Cryostat Microtome. For immunofluorescence on cryosections, brain slices were blocked for 1 h at room temperature in the blocking solution (2% goat serum, 0.2% Triton X-100 in PBS). Subsequently, the sections were incubated with primary antibodies for 2 h at room temperature or 12 h at 4°C, washed 3 times with PBS and incubated with secondary antibodies for 1h, followed by DAPI staining for 10 min at room temperature. Last, sections were mounted in Fluoromount-G for imaging.

SDS-PAGE and western blot: Cells were harvested and lysed in RIPA buffer (1% NP-40, 0.1% SDS, 0.5% sodium deoxycholate, 150 mM NaCl, 25 mM Tris/HCl, pH 7.5, and protease inhibitors). Lysates were clarified by centrifugation (16,000 ×g at 4°C for 15 min), and 20–30 μg protein was separated on SDS-PAGE gels and transferred onto PVDF membranes. Membranes were blocked with 5% BSA, incubated and washed with primary and secondary antibodies. The protein bands were detected with chemiluminescence substrates, and images were captured by the Biorad ChemiDoc system.

Silver staining: The SDS-PAGE gel was washed in ultrapure water, fixed in 30% ethanol:10% acetic acid solution, and washed with 10% ethanol solution and ultrapure water. The gel was then incubated in a sensitizer working solution for exactly 1 min and washed with ultrapure water, followed by incubating in a stain working solution for 30 min. The gel was quickly washed with ultrapure water, immediately added developer working solution, and incubated until protein bands appeared. Last, the gel was stopped by incubating the stop solution (5% acetic acid).

RNA-FISH-combined immunofluorescence (IF) staining: When RNA FISH is combined with IF, we performed IF (under RNase-free conditions) before FISH. Briefly, the freshly PFA-fixed samples were permeabilized for 5min in 0.2% v/v Triton X-100 in PBS containing 2 mM ribonucleoside vanadyl complex (RVC), followed by proteinase K treatment and mock RNA digestion. The samples were then blocked with the blocking buffer, incubated with primary and secondary antibodies, and fixed again. Before RNA FISH, the endogenous biotin or biotinylated proteins in the samples were blocked using the Endogenous Biotin-Blocking Kit. The samples were pre-hybridized for 1–2 h at 42°C, then hybridized overnight with the biotin-conjugated Oligo(dT)20 probe in hybridization buffer and washed with SSC buffer. The samples then went through signal amplification with the Alexa Fluor 488 Tyramide Super Boost Kit. Briefly, samples were incubated with HRP-conjugated streptavidin for 30–60 min at room temperature and treated with tyramide working solution for 3 min. Within this time, HRP converted Alexa Fluor 488-conjugated-tyramide into a highly reactive form that covalently links to tyrosine residues on proteins near HRP. The reaction was stopped by the reaction stop reagent. The tissues were then mounted for imaging.

Lentivirus preparation: To generate lentivirus, HEK293T cells were seeded into a 10 cm dish and later these cells should be >90% confluent at the time of transfection. The cells were transfected with 15 μg lentiviral plasmid, 10 μg psPAX2 plasmid and 5 μg pMD2.G plasmid. 48 h after transfection, the supernatant containing lentivirus was harvested and concentrated with the concentrator solution. The aliquoted virus was then frozen at −80°C.

Immunofluorescence staining on cells: Cells were fixed in 4% PFA for 10 min, permeabilized and blocked with blocking buffer (2% donkey serum, 0.2% triton X-100, in PBS) for 1 h at room temperature. Cells were then incubated with primary antibodies for 1 h at room temperature or 4°C overnight and incubated with secondary antibodies for 1 h, followed by staining in DAPI for 10 min. Finally, cells were mounted on glass slides using Fluoromount G.

Expansion microscopy: Fixed cells with 4% PFA were incubated in primary antibodies and then were fixed in 4% PFA for 20 min. After fixation, cells were incubated in the AcX (Acryloyl-X SE) solution for 2 to 3 h and then polymerized in the gelling solution. The gel was digested with proteinase K for 12 h at room temperature. After digestion, the gel was incubated in the secondary antibody for 2 h at room temperature. The gel was then washed, expanded by four washes with excessive water and mounted on glass slides with superglue.

Quantitative real-time PCR: Total RNAs were extracted using the Trizol reagent. Quantitative PCR was performed in Quantstudio 3 System (Applied Biosystems) with 100 ng total RNA per reaction and qPCR reagents (qScript XLT One-Step RT-qPCR ToughMix, Low ROX). The TaqMan gene expression probes used were Hs05030235_g1 (*MARCKS*), Hs02786624_g1 (*GAPDH*), Mm01210070_g1 (*CKAP2*), Mm00494645_m1 (*GLI1*), Mm00436026_m1 (*PTCH1*) and Mm99999915_g1 (*GAPDH*) to normalize the samples.

For the genotyping analysis of the *detlaARL13B-GFP-TurboID* transgenic mice, quantitative PCR was performed in Quantstudio 3 System with the qPCR reagents (PerfeCTa SYBR Green FastMix Low ROX). The following primers were used for qRT-PCR: transgene (F: 5′-GAATCGGCGAGCTGAAGAGT-3′ and R: 5′-CATTGGGCCATTTGACTCGC-3′), *GAPDH* (F: 5′-AGCCATCAGCTATGCACGTA-3′ and R: 5′-GCCTCGGCTGCTCAAAGAAT-3′). Transcript levels were calculated relative to *GAPDH* using the ΔΔCt method.

Image acquisition: Confocal images were acquired on an LSM880 confocal microscope (Zeiss) and an Olympus IX83 microscope (Evident) equipped with a spinning disk confocal unit (CSU–W1; Andor). Immunofluorescence images of cell lines were imaged on a Leica DMi8 (LAS X software) with Plan Apochromat oil objectives (63x, 1.4 NA). For expansion microscopy, imaging was performed by an AiryScan LSM880 confocal microscope (Zeiss) with a 63x lens. Images related to protein co-localization are from one focal plan. Widefield fluorescence images were acquired on a Leica Mica confocal microscope with a 10x lens. Western blot and silver staining images were acquired on a ChemiDoc MP Imaging System (Bio-Rad).

QUANTIFICATION AND STATISTICAL ANALYSIS

Quantification: For all analyses, the number of replicates is listed in the figure legends. ImageJ software was used for the measurement of brain width, cortex length, axis length, area of cerebella, and cell number. For quantification on cultured cells, 5–10 images for each condition were randomly taken from the coverslips. For cilium quantification, 50–100 cilia from the 5–10 images were counted. Cilium length and protein intensity were measured in Leica LAS X software. For mutant mice, 10 adult mice were used for the measurement of brain size. For quantification of embryonic and postnatal cortex thickness, 6–7 brains were used for each condition. For western blot, quantitation of bands was performed in ImageJ.

Statistical analysis: All statistical tests were performed using GraphPad Prism, and data are presented as means ± SD. All statistical methods are listed in the figure legends. Statistical tests were performed using two–way analysis of variance (ANOVA) with Tukey's multiple comparisons for quantification of ciliary Smo and Gli2 intensity in the cilia and quantitative real-time PCR, and using one-way ANOVA followed by the multiple comparisons (Tukey test) for the analysis of adult mouse brains and quantification of the percentage of ciliated cells, cilia length, *MARCKS* and *CKAP2* RNA levels. For all analyses, statistically significant data are indicated as: *$p < 0.05$, **$p < 0.01$, ***$p < 0.001$, ****$p < 0.0001$. Non-significant data is indicated as ns.

Supplementary Material

Refer to Web version on PubMed Central for supplementary material.

ACKNOWLEDGMENTS

We thank Dr. Rajat Rohatgi (Stanford University) for the gifts of CRISPR-Cas9 reagents and Dr. Matthew Scott's lab for the antibody against SMO. We thank Dr. Shin-ichi Sakakibara (Waseda University) for the antibody against mouse CKAP2L. We thank Dr. David Gravano (Stem Cell Instrumentation Foundry, University of California,

Merced) for fluorescence-activated cell sorting. TurboID is provided by Dr. Alice Ting at Stanford University. The data in this work were collected, in part, with a confocal microscope acquired through the National Science Foundation MRI award no. DMR-1625733. Research in the laboratory of X.G. was supported by NIH/NCI (CA235749), NIH/NIGMS(GM143276), NIH/NCI (CA274595), and NSF CAREER award (IOS-2143711). Research from J.R.Y. laboratory was supported by NIH/NIGMS P41GM103533.

REFERENCES

1. Goetz SC, and Anderson KV (2010). The primary cilium: a signalling centre during vertebrate development. Nat. Rev. Genet 11, 331–344. 10.1038/nrg2774. [PubMed: 20395968]
2. Garcia G 3rd, Raleigh DR, and Reiter JF (2018). How the Ciliary Membrane Is Organized Inside-Out to Communicate Outside-In. Curr. Biol 28, R421–R434. 10.1016/j.cub.2018.03.010. [PubMed: 29689227]
3. Anvarian Z, Mykytyn K, Mukhopadhyay S, Pedersen LB, and Christensen ST (2019). Cellular signalling by primary cilia in development, organ function and disease. Nat. Rev. Nephrol 15, 199–219. 10.1038/s41581-019-0116-9. [PubMed: 30733609]
4. Reiter JF, and Leroux MR (2017). Genes and molecular pathways underpinning ciliopathies. Nat. Rev. Mol. Cell Biol 18, 533–547. 10.1038/nrm.2017.60. [PubMed: 28698599]
5. Valente EM, Rosti RO, Gibbs E, and Gleeson JG (2014). Primary cilia in neurodevelopmental disorders. Nat. Rev. Neurol 10, 27–36. 10.1038/nrneurol.2013.247. [PubMed: 24296655]
6. Liu S, Trupiano MX, Simon J, Guo J, and Anton ES (2021). The essential role of primary cilia in cerebral cortical development and disorders. Curr. Top. Dev. Biol 142, 99–146. 10.1016/bs.ctdb.2020.11.003. [PubMed: 33706927]
7. Cantagrel V, Silhavy JL, Bielas SL, Swistun D, Marsh SE, Bertrand JY, Audollent S, Attié-Bitach T, Holden KR, Dobyns WB, et al. (2008). Mutations in the Cilia Gene ARL13B Lead to the Classical Form of Joubert Syndrome. Am. J. Hum. Genet 83, 170–179. 10.1016/j.ajhg.2008.06.023. [PubMed: 18674751]
8. Bielas SL, Silhavy JL, Brancati F, Kisseleva MV, Al-Gazali L, Sztriha L, Bayoumi RA, Zaki MS, Abdel-Aleem A, Rosti RO, et al. (2009). Mutations in INPP5E, encoding inositol polyphosphate-5-phosphatase E, link phosphatidyl inositol signaling to the ciliopathies. Nat. Genet 41, 1032–1036. 10.1038/ng.423. [PubMed: 19668216]
9. Gabriel E, Wason A, Ramani A, Gooi LM, Keller P, Pozniakovsky A, Poser I, Noack F, Telugu NS, Calegari F, et al. (2016). CPAP promotes timely cilium disassembly to maintain neural progenitor pool. EMBO J. 35, 803–819. 10.15252/embj.201593679. [PubMed: 26929011]
10. Uzquiano A, Cifuentes-Diaz C, Jabali A, Romero DM, Houllier A, Dingli F, Maillard C, Boland A, Deleuze JF, Loew D, et al. (2019). Mutations in the Heterotopia Gene Eml1/EML1 Severely Disrupt the Formation of Primary Cilia. Cell Rep. 28, 1596–1611.e10. 10.1016/j.celrep.2019.06.096. [PubMed: 31390572]
11. Hu WF, Chahrour MH, and Walsh CA (2014). The Diverse Genetic Landscape of Neurodevelopmental Disorders. Annu. Rev. Genomics Hum. Genet 15, 195–213. 10.1146/annurev-genom-090413-025600. [PubMed: 25184530]
12. Paridaen JTML, and Huttner WB (2014). Neurogenesis during development of the vertebrate central nervous system. EMBO Rep. 15, 351–364. 10.1002/embr.201438447. [PubMed: 24639559]
13. Kriegstein A, and Alvarez-Buylla A (2009). The Glial Nature of Embryonic and Adult Neural Stem Cells. Annu. Rev. Neurosci 32, 149–184. 10.1146/annurev.neuro.051508.135600. [PubMed: 19555289]
14. Campbell K, and Götz M (2002). Radial glia: multi-purpose cells for vertebrate brain development. Trends Neurosci. 25, 235–238. 10.1016/s0166-2236(02)02156-2. [PubMed: 11972958]
15. Lehtinen MK, and Walsh CA (2011). Neurogenesis at the Brain–Cerebrospinal Fluid Interface. Annu. Rev. Cell Dev. Biol 27, 653–679. 10.1146/annurev-cellbio-092910-154026. [PubMed: 21801012]
16. Lun MP, Monuki ES, and Lehtinen MK (2015). Development and functions of the choroid plexus–cerebrospinal fluid system. Nat. Rev. Neurosci 16, 445–457. 10.1038/nrn3921. [PubMed: 26174708]

17. Lehtinen MK, Zappaterra MW, Chen X, Yang YJ, Hill AD, Lun M, Maynard T, Gonzalez D, Kim S, Ye P, et al. (2011). The Cerebrospinal Fluid Provides a Proliferative Niche for Neural Progenitor Cells. Neuron 69, 893–905. 10.1016/j.neuron.2011.01.023. [PubMed: 21382550]
18. Malatesta P, Hack MA, Hartfuss E, Kettenmann H, Klinkert W, Kirchhoff F, and Götz M (2003). Neuronal or glial progeny: regional differences in radial glia fate. Neuron 37, 751–764. 10.1016/s0896-6273(03)00116-8. [PubMed: 12628166]
19. Anthony TE, Klein C, Fishell G, and Heintz N (2004). Radial glia serve as neuronal progenitors in all regions of the central nervous system. Neuron 41, 881–890. 10.1016/S0896-6273(04)00140-0. [PubMed: 15046721]
20. Götz M, and Barde YA (2005). Radial glial cells defined and major intermediates between embryonic stem cells and CNS neurons. Neuron 46, 369–372. 10.1016/j.neuron.2005.04.012. [PubMed: 15882633]
21. Pinto L, and Götz M (2007). Radial glial cell heterogeneity–the source of diverse progeny in the CNS. Prog. Neurobiol 83, 2–23. 10.1016/j.pneurobio.2007.02.010. [PubMed: 17580100]
22. Kriegstein AR, and Götz M (2003). Radial glia diversity: A matter of cell fate. Glia 43, 37–43. 10.1002/glia.10250. [PubMed: 12761864]
23. Götz M, and Huttner WB (2005). The cell biology of neurogenesis. Nat. Rev. Mol. Cell Biol 6, 777–788. 10.1038/nrm1739. [PubMed: 16314867]
24. Evsyukova I, Plestant C, and Anton ES (2013). Integrative mechanisms of oriented neuronal migration in the developing brain. Annu. Rev. Cell Dev. Biol 29, 299–353. 10.1146/annurev-cellbio-101512-122400. [PubMed: 23937349]
25. Wonders CP, and Anderson SA (2006). The origin and specification of cortical interneurons. Nat. Rev. Neurosci 7, 687–696. 10.1038/nrn1954. [PubMed: 16883309]
26. Ventura RE, and Goldman JE (2007). Dorsal radial glia generate olfactory bulb interneurons in the postnatal murine brain. J. Neurosci 27, 4297–4302. 10.1523/JNEUROSCI.0399-07.2007. [PubMed: 17442813]
27. Marín O, Valiente M, Ge X, and Tsai LH (2010). Guiding neuronal cell migrations. Cold Spring Harbor Perspect. Biol 2, a001834.
28. Panchision DM, and McKay RDG (2002). The control of neural stem cells by morphogenic signals. Curr. Opin. Genet. Dev 12, 478–487. 10.1016/s0959-437x(02)00329-5. [PubMed: 12100896]
29. Fode C, Ma Q, Casarosa S, Ang SL, Anderson DJ, and Guillemot F (2000). A role for neural determination genes in specifying the dorsoventral identity of telencephalic neurons. Genes Dev. 14, 67–80. [PubMed: 10640277]
30. Edlund T, and Jessell TM (1999). Progression from extrinsic to intrinsic signaling in cell fate specification: a view from the nervous system. Cell 96, 211–224. 10.1016/s0092-8674(00)80561-9. [PubMed: 9988216]
31. Mick DU, Rodrigues RB, Leib RD, Adams CM, Chien AS, Gygi SP, and Nachury MV (2015). Proteomics of Primary Cilia by Proximity Labeling. Dev. Cell 35, 497–512. 10.1016/j.devcel.2015.10.015. [PubMed: 26585297]
32. May EA, Kalocsay M, D'Auriac IG, Schuster PS, Gygi SP, Nachury MV, and Mick DU (2021). Time-resolved proteomics profiling of the ciliary Hedgehog response. JCB (J. Cell Biol.) 220, e202007207. [PubMed: 33856408]
33. Liu X, Yam PT, Schlienger S, Cai E, Zhang J, Chen WJ, Torres Gutierrez O, Jimenez Amilburu V, Ramamurthy V, Ting AY, et al. (2024). Numb positively regulates Hedgehog signaling at the ciliary pocket. Nat. Commun 15, 3365. 10.1038/s41467-024-47244-1. [PubMed: 38664376]
34. Ding S, Xu T, and Wu X (2014). Generation of genetically engineered mice by the piggyBac transposon system. Methods Mol. Biol 1194, 171–185. 10.1007/978-1-4939-1215-5_9.
35. Feng L, Hatten ME, and Heintz N (1994). Brain lipid-binding protein (BLBP): A novel signaling system in the developing mammalian CNS. Neuron 12, 895–908. 10.1016/0896-6273(94)90341-7. [PubMed: 8161459]
36. Kurtz A, Zimmer A, Schnütgen F, Brüning G, Spener F, and Müller T (1994). The expression pattern of a novel gene encoding brain-fatty acid binding protein correlates with neuronal and glial

cell development. Development (Cambridge, England) 120, 2637–2649. 10.1242/dev.120.9.2637. [PubMed: 7956838]

37. Meyer SC, Gaj T, and Ghosh I (2006). Highly selective cyclic peptide ligands for NeutrAvidin and avidin identified by phage display. Chem. Biol. Drug Des 68, 3–10. 10.1111/j.1747-0285.2006.00401.x. [PubMed: 16923020]
38. Nguyen TT, Sly KL, and Conboy JC (2012). Comparison of the energetics of avidin, streptavidin, neutrAvidin, and anti-biotin antibody binding to biotinylated lipid bilayer examined by second-harmonic generation. Anal. Chem 84, 201–208. 10.1021/ac202375n. [PubMed: 22122646]
39. Alon R, Bayer EA, and Wilchek M (1992). Cell-adhesive properties of streptavidin are mediated by the exposure of an RGD-like RYD site. Eur. J. Cell Biol 58, 271–279. [PubMed: 1425765]
40. Storey JD, and Tibshirani R (2003). Statistical significance for genomewide studies. Proc. Natl. Acad. Sci. USA 100, 9440–9445. 10.1073/pnas.1530509100. [PubMed: 12883005]
41. Ishikawa H, Thompson J, Yates JR 3rd, and Marshall WF (2012). Proteomic analysis of mammalian primary cilia. Curr. Biol 22, 414–419. 10.1016/j.cub.2012.01.031. [PubMed: 22326026]
42. Kohli P, Höhne M, Jüngst C, Bertsch S, Ebert LK, Schauss AC, Benzing T, Rinschen MM, and Schermer B (2017). The ciliary membrane-associated proteome reveals actin-binding proteins as key components of cilia. EMBO Rep. 18, 1521–1535. 10.15252/embr.201643846. [PubMed: 28710093]
43. Hao K, Chen Y, Yan X, and Zhu X (2021). Cilia locally synthesize proteins to sustain their ultrastructure and functions. Nat. Commun 12, 6971. 10.1038/s41467-021-27298-1. [PubMed: 34848703]
44. Leblond CS, Le TL, Malesys S, Cliquet F, Tabet AC, Delorme R, Rolland T, and Bourgeron T (2021). Operative list of genes associated with autism and neurodevelopmental disorders based on database review. Mol. Cell. Neurosci 113, 103623. 10.1016/j.mcn.2021.103623. [PubMed: 33932580]
45. Albert KA, Wu WC, Nairn AC, and Greengard P (1984). Inhibition by calmodulin of calcium/phospholipid-dependent protein phosphorylation. Proc. Natl. Acad. Sci. USA 81, 3622–3625. 10.1073/pnas.81.12.3622. [PubMed: 6233611]
46. Wu WC, Walaas SI, Nairn AC, and Greengard P (1982). Calcium/phospholipid regulates phosphorylation of a Mr “87k” substrate protein in brain synaptosomes. Proc. Natl. Acad. Sci. USA 79, 5249–5253. 10.1073/pnas.79.17.5249. [PubMed: 6957862]
47. Stumpo DJ, Bock CB, Tuttle JS, and Blackshear PJ (1995). MARCKS deficiency in mice leads to abnormal brain development and perinatal death. Proc. Natl. Acad. Sci. USA 92, 944–948. 10.1073/pnas.92.4.944. [PubMed: 7862670]
48. Blackshear PJ, Lai WS, Tuttle JS, Stumpo DJ, Kennington E, Nairn AC, and Sulik KK (1996). Developmental expression of MARCKS and protein kinase C in mice in relation to the exencephaly resulting from MARCKS deficiency. Brain Res. Dev. Brain Res 96, 62–75. 10.1016/0165-3806(96)00097-1. [PubMed: 8922669]
49. Weimer JM, Yokota Y, Stanco A, Stumpo DJ, Blackshear PJ, and Anton ES (2009). MARCKS modulates radial progenitor placement, proliferation and organization in the developing cerebral cortex. Development 136, 2965–2975. 10.1242/dev.036616. [PubMed: 19666823]
50. Aparicio G, Arruti C, and Zolessi FR (2018). MARCKS phosphorylation by PKC strongly impairs cell polarity in the chick neural plate. Genesis 56, e23104. 10.1002/dvg.23104. [PubMed: 29603589]
51. Deichaite I, Casson LP, Ling HP, and Resh MD (1988). In vitro synthesis of pp60v-src: myristylation in a cell-free system. Mol. Cell Biol 8, 4295–4301. 10.1128/mcb.8.10.4295-4301.1988. [PubMed: 3141787]
52. Graff JM, Gordon JI, and Blackshear PJ (1989). Myristoylated and nonmyristoylated forms of a protein are phosphorylated by protein kinase C. Science 246, 503–506. 10.1126/science.2814478. [PubMed: 2814478]
53. George DJ, and Blackshear PJ (1992). Membrane association of the myristoylated alanine-rich C kinase substrate (MARCKS) protein appears to involve myristate-dependent binding in the absence of a myristoyl protein receptor. J. Biol. Chem 267, 24879–24885. [PubMed: 1332970]

54. Herget T, Oehrlein SA, Pappin DJ, Rozengurt E, and Parker PJ (1995). The myristoylated alanine-rich C-kinase substrate (MARCKS) is sequentially phosphorylated by conventional, novel and atypical isotypes of protein kinase C. Eur. J. Biochem 233, 448–457. 10.1111/j.1432-1033.1995.448_2.x. [PubMed: 7588787]
55. Zuo X, Fogelgren B, and Lipschutz JH (2011). The small GTPase Cdc42 is necessary for primary ciliogenesis in renal tubular epithelial cells. J. Biol. Chem 286, 22469–22477. 10.1074/jbc.M111.238469. [PubMed: 21543338]
56. Choi SY, Chacon-Heszele MF, Huang L, McKenna S, Wilson FP, Zuo X, and Lipschutz JH (2013). Cdc42 deficiency causes ciliary abnormalities and cystic kidneys. J. Am. Soc. Nephrol 24, 1435–1450. 10.1681/ASN.2012121236. [PubMed: 23766535]
57. Choi SY, Baek JI, Zuo X, Kim SH, Dunaief JL, and Lipschutz JH (2015). Cdc42 and sec10 Are Required for Normal Retinal Development in Zebrafish. Investig. Ophthalmol. Vis. Sci 56, 3361–3370. 10.1167/iovs.14-15692. [PubMed: 26024121]
58. Hussain MS, Battaglia A, Szczepanski S, Kaygusuz E, Toliat MR, Sakakibara SI, Altmüller J, Thiele H, Nürnberg G, Moosa S, et al. (2014). Mutations in CKAP2L, the human homolog of the mouse radmis gene, cause filippi syndrome. Am. J. Hum. Genet 95, 622–632. 10.1016/j.ajhg.2014.10.008. [PubMed: 25439729]
59. Capecchi G, Baldassarri M, Ferranti S, Guidoni E, Cioni M, Nürnberg P, Mencarelli MA, Renieri A, and Grosso S (2018). CKAP2L mutation confirms the diagnosis of Filippi syndrome. Clin. Genet 93, 1109–1110. 10.1111/cge.13188. [PubMed: 29473684]
60. Karakaya T, Bilgic AE, Eris D, Baser B, Mermer S, and Yildiz O (2021). Identification of a novel pathogenic variant in CKAP2L and literature review in a child with Filippi syndrome and congenital talipes equinovarus. Am. J. Med. Genet 185, 2198–2203. 10.1002/ajmg.a.62223. [PubMed: 33913579]
61. Patrick RJ, Weimer J, Davis-Keppen L, and Landsverk ML (2022). Novel variants identified in CKAP2L in two siblings with Filippi syndrome. Cold Spring Harb. Mol. Case Stud 8, a006130. 10.1101/mcs.a006130. [PubMed: 34921061]
62. Yang XR, and Marwaha A (2022). Expansion of the neurodevelopmental phenotypic spectrum of CKAP2L-related Filippi syndrome to include an adolescent male with normal intellect. Am. J. Med. Genet 188, 1928–1929. 10.1002/ajmg.a.62702. [PubMed: 35224850]
63. Bas H, Durmaz CD, Tombak MC, Cetin GO, and Karaer K (2024). Filippi syndrome: Three new families suggest that urinary system abnormalities may belong to clinical spectrum of the disease. Am. J. Med. Genet 194, e63654. 10.1002/ajmg.a.63654. [PubMed: 38738944]
64. Yumoto T, Nakadate K, Nakamura Y, Sugitani Y, Sugitani-Yoshida R, Ueda S, and Sakakibara SI (2013). Radmis, a novel mitotic spindle protein that functions in cell division of neural progenitors. PLoS One 8, e79895. 10.1371/journal.pone.0079895. [PubMed: 24260314]
65. Kwon H, Joh JY, and Hong KU (2024). Human CKAP2L shows a cell cycle-dependent expression pattern and exhibits microtubule-stabilizing properties. FEBS Open Bio 14, 1526–1539. 10.1002/2211-5463.13864.
66. Niida Y, Togi S, and Ura H (2021). Molecular Bases of Human Malformation Syndromes Involving the SHH Pathway: GLIA/R Balance and Cardinal Phenotypes. Int. J. Mol. Sci 22, 13060. 10.3390/ijms222313060. [PubMed: 34884862]
67. Kim J, Kato M, and Beachy PA (2009). Gli2 trafficking links Hedgehog-dependent activation of Smoothened in the primary cilium to transcriptional activation in the nucleus. Proc. Natl. Acad. Sci. USA 106, 21666–21671. 10.1073/pnas.0912180106. [PubMed: 19996169]
68. Wang H, Ge G, Uchida Y, Luu B, and Ahn S (2011). Gli3 is Required for Maintenance and Fate Specification of Cortical Progenitors. J. Neurosci 31, 6440–6448. 10.1523/JNEUROSCI.4892-10.2011. [PubMed: 21525285]
69. Motoyama J, Milenkovic L, Iwama M, Shikata Y, Scott MP, and Hui CC (2003). Differential requirement for Gli2 and Gli3 in ventral neural cell fate specification. Dev. Biol 259, 150–161. 10.1016/s0012-1606(03)00159-3. [PubMed: 12812795]
70. Theil T, Alvarez-Bolado G, Walter A, and Rüther U (1999). Gli3 is required for Emx gene expression during dorsal telencephalon development. Development (Cambridge, England) 126, 3561–3571. 10.1242/dev.126.16.3561. [PubMed: 10409502]

71. Komada M, Saitsu H, Kinboshi M, Miura T, Shiota K, and Ishibashi M (2008). Hedgehog signaling is involved in development of the neocortex. Development 135, 2717–2727. 10.1242/dev.015891. [PubMed: 18614579]

72. Machold R, Hayashi S, Rutlin M, Muzumdar MD, Nery S, Corbin JG, Gritli-Linde A, Dellovade T, Porter JA, Rubin LL, et al. (2003). Sonic hedgehog is required for progenitor cell maintenance in telencephalic stem cell niches. Neuron 39, 937–950. 10.1016/s0896-6273(03)00561-0. [PubMed: 12971894]

73. Wechsler-Reya RJ, and Scott MP (1999). Control of Neuronal Precursor Proliferation in the Cerebellum by Sonic Hedgehog. Neuron 22, 103–114. 10.1016/S0896-6273(00)80682-0. [PubMed: 10027293]

74. Wallace VA (1999). Purkinje-cell-derived Sonic hedgehog regulates granule neuron precursor cell proliferation in the developing mouse cerebellum. Curr. Biol 9, 445–448. 10.1016/S0960-9822(99)80195-X. [PubMed: 10226030]

75. Dahmane N, and Ruiz-i-Altaba A (1999). Sonic hedgehog regulates the growth and patterning of the cerebellum. Development 126, 3089–3100. 10.1242/dev.126.14.3089. [PubMed: 10375501]

76. Hong KU, Park YS, Seong YS, Kang D, Bae CD, and Park J (2007). Functional importance of the anaphase-promoting complex-Cdh1-mediated degradation of TMAP/CKAP2 in regulation of spindle function and cytokinesis. Mol. Cell Biol 27, 3667–3681. 10.1128/MCB.01386-06. [PubMed: 17339342]

77. Seki A, and Fang G (2007). CKAP2 is a spindle-associated protein degraded by APC/C-Cdh1 during mitotic exit. J. Biol. Chem 282, 15103–15113. 10.1074/jbc.M701688200. [PubMed: 17376772]

78. Gupta GD, Coyaud É, Gonçalves J, Mojarad BA, Liu Y, Wu Q, Gheiratmand L, Comartin D, Tkach JM, Cheung SWT, et al. (2015). A Dynamic Protein Interaction Landscape of the Human Centrosome-Cilium Interface. Cell 163, 1484–1499. 10.1016/j.cell.2015.10.065. [PubMed: 26638075]

79. Aslanyan MG, Doornbos C, Diwan GD, Anvarian Z, Beyer T, Junger K, van Beersum SEC, Russell RB, Ueffing M, Ludwig A, et al. (2023). A targeted multi-proteomics approach generates a blueprint of the ciliary ubiquitinome. Front. Cell Dev. Biol 11, 1113656. 10.3389/fcell.2023.1113656. [PubMed: 36776558]

80. Schneider L, Clement CA, Teilmann SC, Pazour GJ, Hoffmann EK, Satir P, and Christensen ST (2005). PDGFRalphaalpha signaling is regulated through the primary cilium in fibroblasts. Curr. Biol 15, 1861–1866. 10.1016/j.cub.2005.09.012. [PubMed: 16243034]

81. Clement DL, Mally S, Stock C, Lethan M, Satir P, Schwab A, Pedersen SF, and Christensen ST (2013). PDGFRalpha signaling in the primary cilium regulates NHE1-dependent fibroblast migration via coordinated differential activity of MEK1/2-ERK1/2-p90RSK and AKT signaling pathways. J. Cell Sci 126, 953–965. 10.1242/jcs.116426. [PubMed: 23264740]

82. Loktev AV, and Jackson PK (2013). Neuropeptide Y family receptors traffic via the Bardet-Biedl syndrome pathway to signal in neuronal primary cilia. Cell Rep. 5, 1316–1329. 10.1016/j.celrep.2013.11.011. [PubMed: 24316073]

83. Corbit KC, Aanstad P, Singla V, Norman AR, Stainier DYR, and Reiter JF (2005). Vertebrate Smoothened functions at the primary cilium. Nature 437, 1018–1021. 10.1038/nature04117. [PubMed: 16136078]

84. Rohatgi R, Milenkovic L, and Scott MP (2007). Patched1 regulates hedgehog signaling at the primary cilium. Science 317, 372–376. 10.1126/science.1139740. [PubMed: 17641202]

85. Sigg MA, Menchen T, Lee C, Johnson J, Jungnickel MK, Choksi SP, Garcia G 3rd, Busengdal H, Dougherty GW, Pennekamp P, et al. (2017). Evolutionary Proteomics Uncovers Ancient Associations of Cilia with Signaling Pathways. Dev. Cell 43, 744–762.e11. 10.1016/j.devcel.2017.11.014. [PubMed: 29257953]

86. Klena N, and Pigino G (2022). Structural Biology of Cilia and Intraflagellar Transport. Annu. Rev. Cell Dev. Biol 38, 103–123. 10.1146/annurev-cellbio-120219-034238. [PubMed: 35767872]

87. Gildea DE, Luetkemeier ES, Bao X, Loftus SK, Mackem S, Yang Y, Pavan WJ, and Biesecker LG (2011). The pleiotropic mouse phenotype extra-toes spotting is caused by translation initiation

factor Eif3c mutations and is associated with disrupted sonic hedgehog signaling. FASEB J. 25, 1596–1605. 10.1096/fj.10-169771. [PubMed: 21292980]

88. Fujii K, Zhulyn O, Byeon GW, Genuth NR, Kerr CH, Walsh EM, and Barna M (2021). Controlling tissue patterning by translational regulation of signaling transcripts through the core translation factor eIF3c. Dev. Cell 56, 2928–2937.e9. 10.1016/j.devcel.2021.10.009. [PubMed: 34752747]
89. Holt CE, Martin KC, and Schuman EM (2019). Local translation in neurons: visualization and function. Nat. Struct. Mol. Biol 26, 557–566. 10.1038/s41594-019-0263-5. [PubMed: 31270476]
90. Holt CE, and Schuman EM (2013). The central dogma decentralized: new perspectives on RNA function and local translation in neurons. Neuron 80, 648–657. 10.1016/j.neuron.2013.10.036. [PubMed: 24183017]
91. Pfeiffer BE, and Huber KM (2006). Current advances in local protein synthesis and synaptic plasticity. J. Neurosci 26, 7147–7150. 10.1523/JNEUROSCI.1797-06.2006. [PubMed: 16822970]
92. Tomé D, and Almeida RD (2024). The injured axon: intrinsic mechanisms driving axonal regeneration. Trends Neurosci. 47, 875–891. 10.1016/j.tins.2024.09.009. [PubMed: 39438216]
93. Sauer ME, and Walker BE (1959). Radioautographic study of interkinetic nuclear migration in the neural tube. Proc. Soc. Exp. Biol. Med 101, 557–560. 10.3181/00379727-101-25014. [PubMed: 13675315]
94. Kosodo Y (2012). Interkinetic nuclear migration: beyond a hallmark of neurogenesis. Cell. Mol. Life Sci 69, 2727–2738. 10.1007/s00018-012-0952-2. [PubMed: 22415322]
95. Prieto D, and Zolessi FR (2017). Functional Diversification of the Four MARCKS Family Members in Zebrafish Neural Development. J. Exp. Zool. B Mol. Dev. Evol 328, 119–138. 10.1002/jez.b.22691. [PubMed: 27554589]
96. Higginbotham H, Guo J, Yokota Y, Umberger NL, Su C-Y, Li J, Verma N, Hirt J, Ghukasyan V, Caspary T, and Anton ES (2013). Arl13b-regulated cilia activities are essential for polarized radial glial scaffold formation. Nat. Neurosci 16, 1000–1007. 10.1038/nn.3451. [PubMed: 23817546]
97. Guo J, Higginbotham H, Li J, Nichols J, Hirt J, Ghukasyan V, and Anton ES (2015). Developmental disruptions underlying brain abnormalities in ciliopathies. Nat. Commun 6, 7857. 10.1038/ncomms8857. [PubMed: 26206566]
98. El Amri M, Fitzgerald U, and Schlosser G (2018). MARCKS and MARCKS-like proteins in development and regeneration. J. Biomed. Sci 25, 43. 10.1186/s12929-018-0445-1. [PubMed: 29788979]
99. Hartwig JH, Thelen M, Rosen A, Janmey PA, Nairn AC, and Aderem A (1992). MARCKS is an actin filament crosslinking protein regulated by protein kinase C and calcium-calmodulin. Nature 356, 618–622. 10.1038/356618a0. [PubMed: 1560845]
100. Sundaram M, Cook HW, and Byers DM (2004). The MARCKS family of phospholipid binding proteins: regulation of phospholipase D and other cellular components. Biochem. Cell. Biol 82, 191–200. 10.1139/o03-087. [PubMed: 15052337]
101. Brudvig JJ, and Weimer JM (2015). X MARCKS the spot: myristoylated alanine-rich C kinase substrate in neuronal function and disease. Front. Cell. Neurosci 9, 407. 10.3389/fncel.2015.00407. [PubMed: 26528135]
102. Trovò L, Ahmed T, Callaerts-Vegh Z, Buzzi A, Bagni C, Chuah M, Vandendriessche T, D'Hooge R, Balschun D, and Dotti CG (2013). Low hippocampal $PI(4,5)P_2$ contributes to reduced cognition in old mice as a result of loss of MARCKS. Nat. Neurosci 16, 449–455. 10.1038/nn.3342. [PubMed: 23434911]
103. Calabrese B, and Halpain S (2005). Essential role for the PKC target MARCKS in maintaining dendritic spine morphology. Neuron 48, 77–90. 10.1016/j.neuron.2005.08.027. [PubMed: 16202710]
104. Theis T, Mishra B, von der Ohe M, Loers G, Prondzynski M, Pless O, Blackshear PJ, Schachner M, and Kleene R (2013). Functional role of the interaction between polysialic acid and myristoylated alanine-rich C kinase substrate at the plasma membrane. J. Biol. Chem 288, 6726–6742. 10.1074/jbc.M112.444034. [PubMed: 23329829]
105. Tanabe A, Shiraishi M, Negishi M, Saito N, Tanabe M, and Sasaki Y (2012). MARCKS dephosphorylation is involved in bradykinin-induced neurite outgrowth in neuroblastoma SH-SY5Y cells. J. Cell. Physiol 227, 618–629. 10.1002/jcp.22763. [PubMed: 21448919]

106. Patten I, and Placzek M (2000). The role of Sonic hedgehog in neural tube patterning. Cell. Mol. Life Sci 57, 1695–1708. 10.1007/PL00000652. [PubMed: 11130176]

107. He L, Diedrich J, Chu YY, and Yates JR 3rd. (2015). Extracting Accurate Precursor Information for Tandem Mass Spectra by Raw-Converter. Anal. Chem 87, 11361–11367. 10.1021/acs.analchem.5b02721. [PubMed: 26499134]

108. Xu T, Park SK, Venable JD, Wohlschlegel JA, Diedrich JK, Cociorva D, Lu B, Liao L, Hewel J, Han X, et al. (2015). ProLuCID: An improved SEQUEST-like algorithm with enhanced sensitivity and specificity. J. Proteomics 129, 16–24. 10.1016/j.jprot.2015.07.001. [PubMed: 26171723]

109. Tabb DL, McDonald WH, and Yates JR 3rd. (2002). DTASelect and Contrast: tools for assembling and comparing protein identifications from shotgun proteomics. J. Proteome Res 1, 21–26. 10.1021/pr015504q. [PubMed: 12643522]

110. Peng J, Elias JE, Thoreen CC, Licklider LJ, and Gygi SP (2003). Evaluation of multidimensional chromatography coupled with tandem mass spectrometry (LC/LC-MS/MS) for large-scale protein analysis: the yeast proteome. J. Proteome Res 2, 43–50. 10.1021/pr025556v. [PubMed: 12643542]

111. Park SK, Venable JD, Xu T, and Yates JR 3rd. (2008). A quantitative analysis software tool for mass spectrometry-based proteomics. Nat. Methods 5, 319–322. 10.1038/nmeth.1195. [PubMed: 18345006]

Highlights

- *In vivo* proteomics with TurboID transgenic mice maps radial glial ciliary proteins
- Radial glial primary cilia contain translation machinery proteins
- Ciliary components exhibit region-specific variations in the dorsal and ventral telencephalon
- Mechanistic studies on MARCKS and CKAP2L reveal new ciliary roles in neurodevelopment

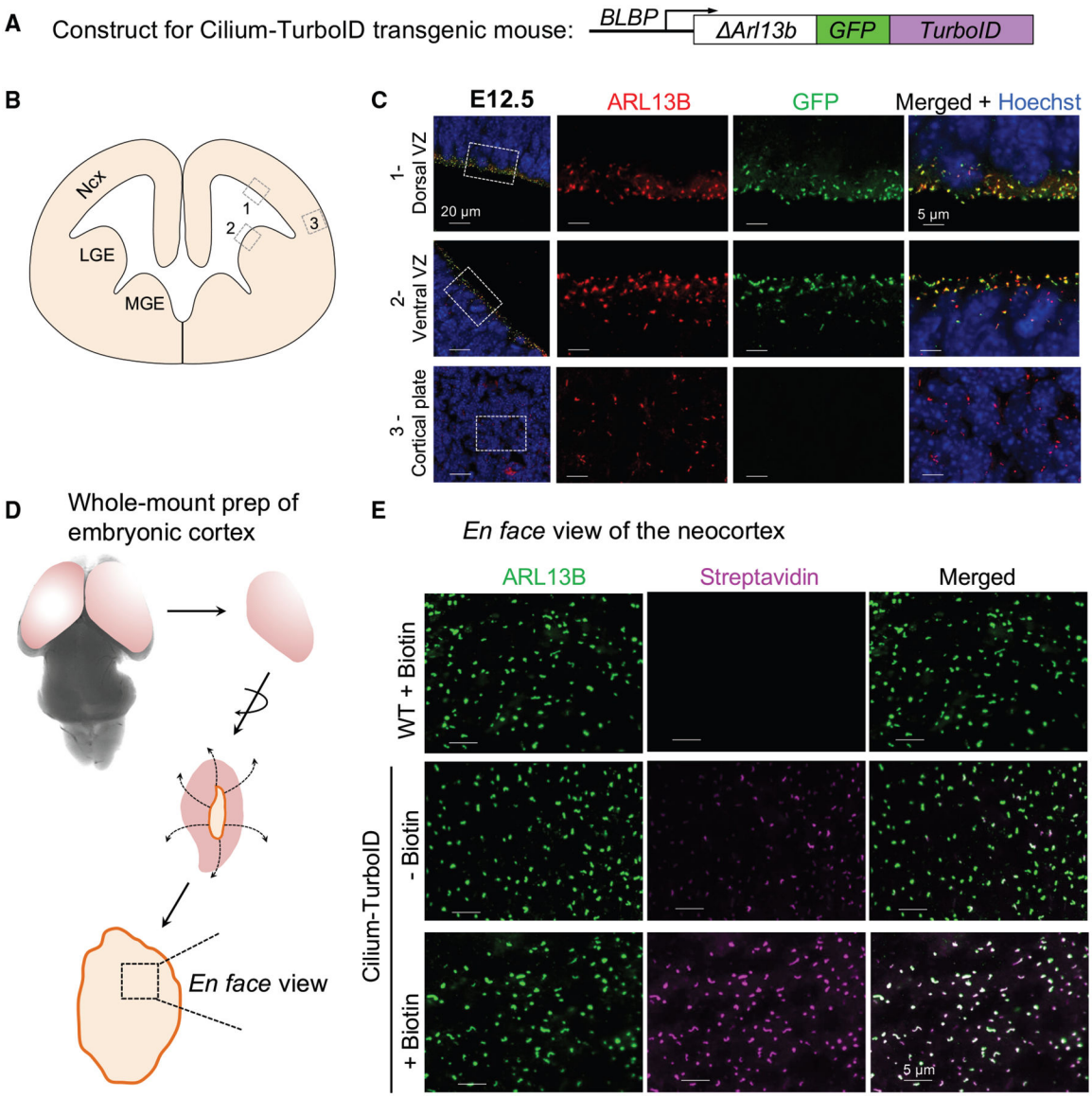

Figure 1. Construction of the mouse model for *in vivo* biotinylation of ciliary proteins in RG in the developing telencephalon

(A) The schematic of the transgenic construct used for the generation of the Cilium-TurboID mouse model. The transgene is expressed as one fused protein of ΔARL13B-GFP-TurboID. ΔARL13B is a truncated form of ARL13B, containing only the N+RVEP+PR domain of ARL13B.

(B) The schematic of the embryonic brain section. Ncx, neocortex; LGE, lateral ganglionic eminence; MGE, medial ganglionic eminence.

(C) Immunofluorescence of cortical sections from dorsal and ventral telencephalon of E12.5 Cilium-TurboID transgenic embryos. The transgene was detected by immunostaining for GFP (green); cilia are labeled by ARL13B (red); DNA is visualized by Hoechst staining (blue). Areas highlighted by gray dashed boxes in different regions are magnified and displayed on the right side.

(D) Diagram illustrating the whole-mount preparation of the embryonic cortex. The two hemispheres are separated, and the hemispheres are cut radially around the ventral opening. The inner surface of the cortex was imaged directly from an *en face* perspective.
(E) Whole-mount staining of transgenic mouse neocortex expressing Cilium-TurboID or WT mouse neocortex before and after biotin labeling. E12.5 brains were incubated with 50 μM biotin for 15 min at 37°C and fixed for immunostaining. The cilium is labeled by ARL13B (green), and the biotinylated proteins were labeled by streptavidin-Alexa Fluor 647 (magenta).
Scale bars, 5 μm in (C) and (E).

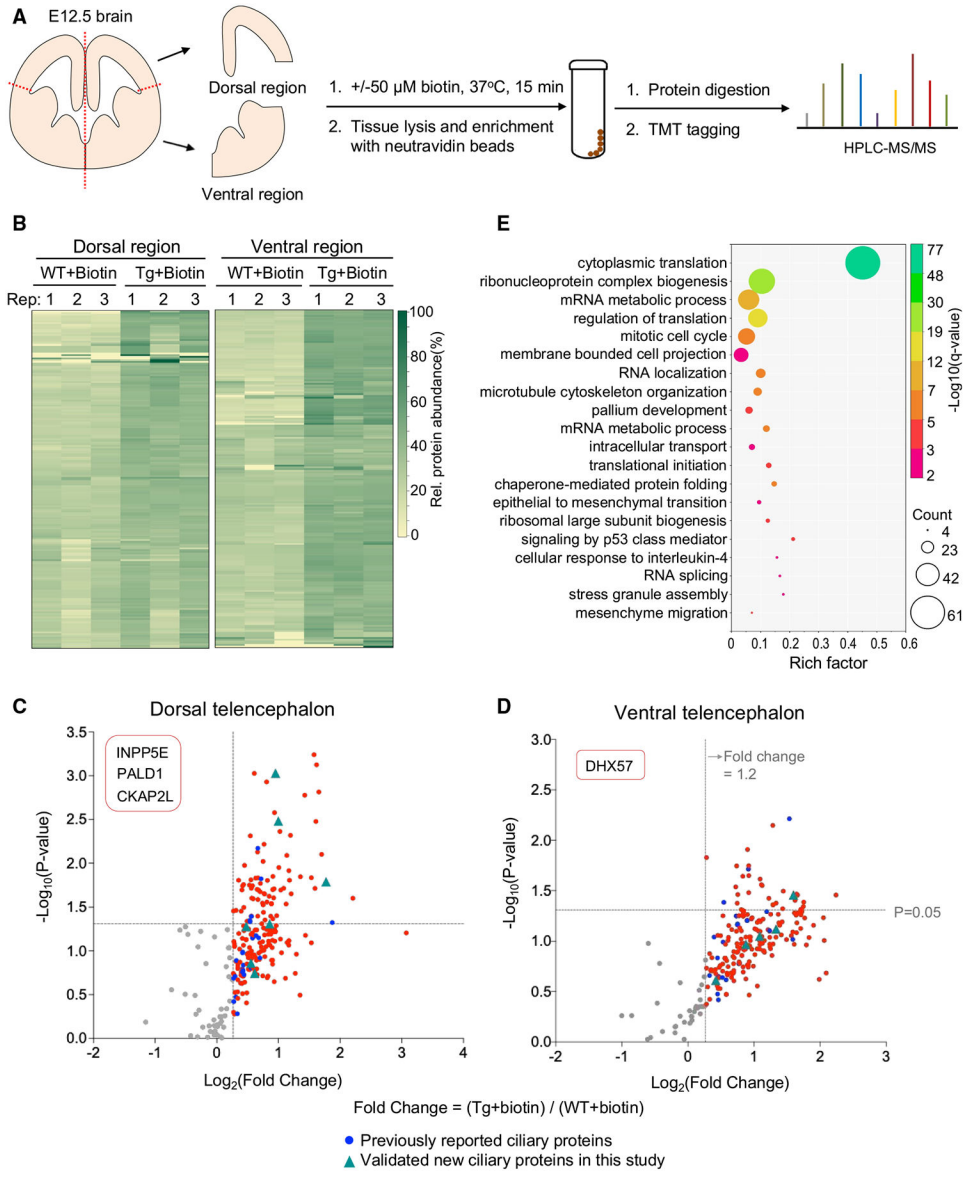

Figure 2. *In vivo* ciliary proteomics of the mouse embryonic telencephalon

(A) Workflow of *in vivo* ciliary proteomic study in the mouse embryonic telencephalon. For each brain, one hemisphere was used for biotin labeling, and the other for vehicle control. The dorsal and ventral regions are separated and processed in parallel. See also Figure S1.

(B) Heatmap of the relative abundance of ciliary candidates in the dorsal and ventral telencephalon. Clustering of the relative abundances of each identified protein (rows) in individual samples (columns) was performed based on Ward's minimum variance method. The relative abundance was calculated within one set of samples that contains all three conditions. The image on the right side indicates the color scheme of relative abundances (percentage).

(C and D) Volcano plot depicting statistical significance versus the fold-change of ciliary candidates from the dorsal (C) and ventral (D) telencephalon. The enrichment ratio was determined by comparing the integrated intensity of proteins in the biotin-labeled transgenic

brain to that in the WT brain. Candidates in the red square next to the *y* axis (INPP5E, PALD1, CKAP2L, and DHX57) were exclusively detected in the transgenic brain and absent in the WT brain. See also Figure S2 and Table S1.

(E) GO enrichment analysis of biological processes was plotted according to the rich factor in Metascape. The top 20 enriched biological processes are represented in the bubble plot.

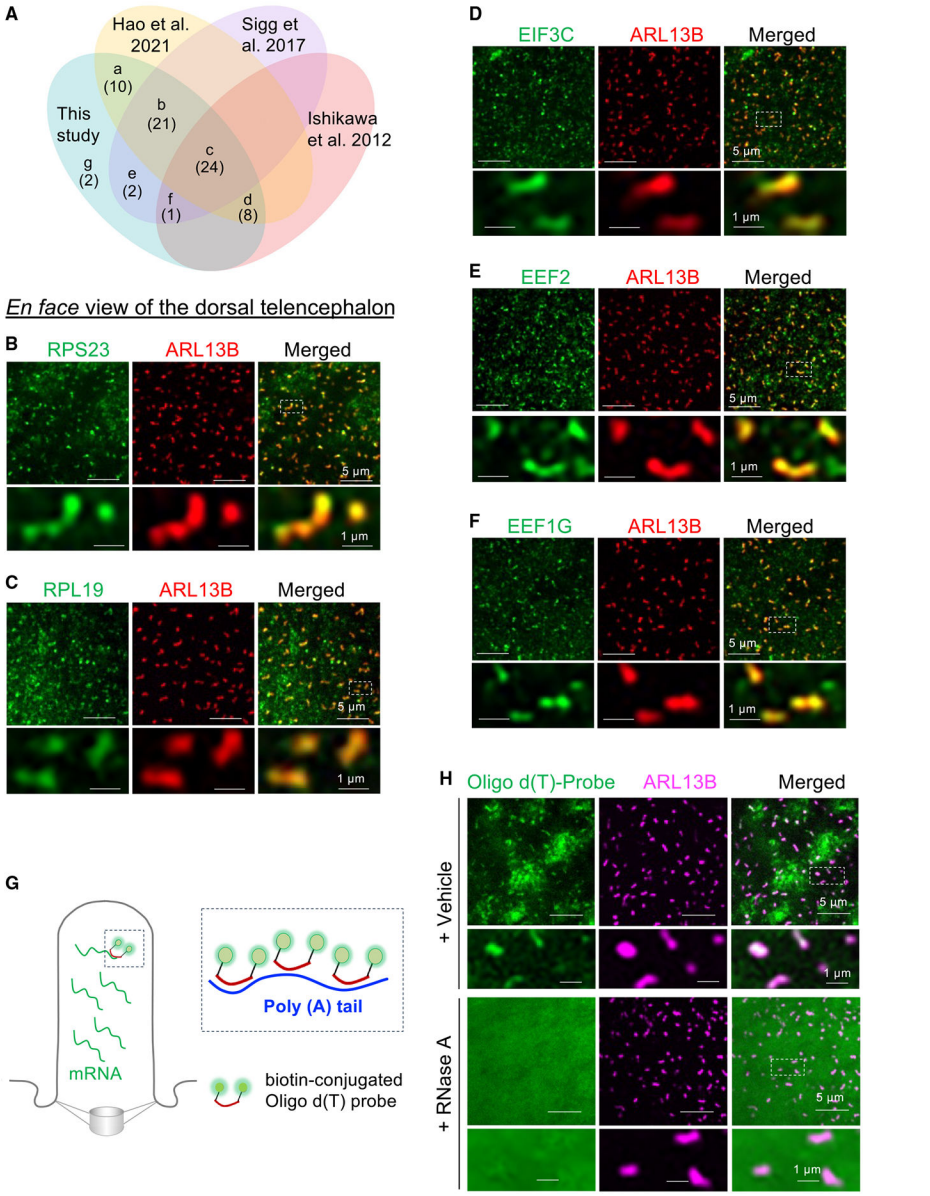

Figure 3. Brain proteomics reveals components of translation machinery in the cilia of radial glia

(A) Venn diagram showing the overlapping of translation machinery components identified in three previous ciliary proteomic studies and our current study. See also Figure S3 and Table S2.

(B–F) *En face* view of the dorsal cortex in the whole-mount E12.5 wild-type (WT) mouse brain. The brain tissues were immuno-stained with antibodies against the indicated translation machinery proteins. Primary cilia are labeled with ARL13B (red). Regions within the white dashed boxes are magnified and shown in the images below. See also Figure S4.

(G) Diagram illustrating fluorescence *in situ* hybridization (FISH) of ciliary mRNA using oligo-d (T) probes conjugated with biotin. The signaling was detected via tyramide signal amplification (TSA).

(H) Representative images of FISH on whole-mount E12.5 WT mouse cortices. Cilia were imaged from an *en face* perspective. Immunostaining with ARL13B was performed to highlight the cilium (magenta). Regions within the white dashed boxes are magnified and shown in the images below. Scale bars, 5 μm (main images) and 1 μm (enlarged insets).

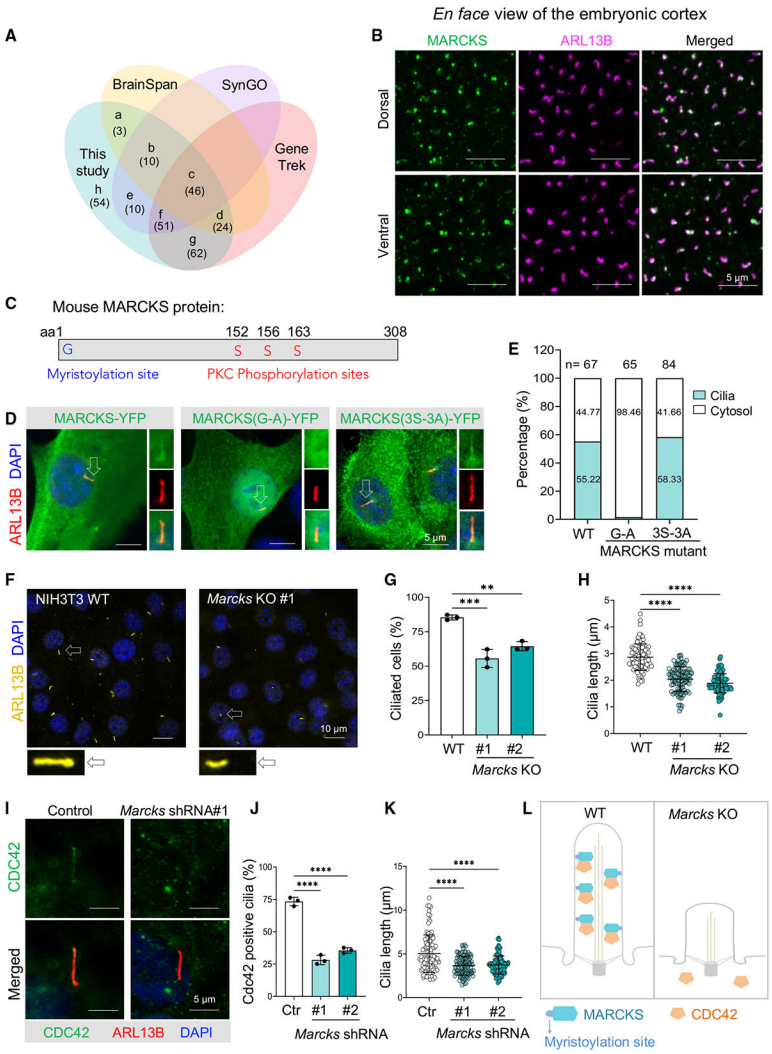

Figure 4. *In vivo* ciliary proteomics identifies a ciliary mechanism of MARCKS, a protein associated with neurodevelopmental disorders

(A) *Venn* diagram showing common proteins shared in our brain ciliary proteomic datasets and the other three curated databases. See also Table S3.

(B) Representative images showing that endogenous MARCKS proteins are present in the primary cilia of E12.5 WT mouse cortex in both the dorsal and ventral regions. Scale bars, 5 μm.

(C) A schematic of the full-length MARCKS protein, with the myristoylation site and PKC phosphorylation sites highlighted.

(D) Myristoylation is required for the cilium localization of MARCKS in NIH3T3 cells. YFP-tagged WT or mutated MARCKS were expressed in NIH3T3, and their subcellular localization was determined by immunofluorescence staining. The cilium pointed by the white arrow is magnified and displayed on the right side. Scale bars, 5 μm.

(E) Quantification of cilium localization for WT and mutant MARCKS. The total number of cells quantified for each condition is listed in the histogram. The experiment was performed 3 times with similar results.

(F) Representative images of cilium staining with ARL13B antibody in WT or *Marcks* KO cells. The cilium pointed by the white arrow is magnified and displayed at the bottom. Scale bars, 10 μm.

(G and H) Quantification of ciliation rate (G) and cilium length (F) in WT or *Marcks* KO cells. At least 100 cilia were quantified for each condition from three replicates. Experiments were performed 3 times with similar results. Data are presented as mean ± SD. Statistics: One-way ANOVA with multiple comparisons (Tukey test). $^{**}p < 0.01$; $^{***}p < 0.001$; $^{****}p < 0.0001$.

(I) Representative images showing ciliary CDC42 levels in control and *Marcks* knockdown ARPE-19 cells. Cells were infected with lentiviruses expressing shRNA targeting *Marcks*. Three days post-infection, cells were serum-starved for 48 h to induce ciliogenesis, followed by immunofluorescence staining. The displayed images were captured from a single focal plane in confocal microscopy. Scale bars, 5 μm.

(J) Quantification of cilia that are positive for CDC42 immunofluorescence signal in WT or *Marcks* knockdown ARPE-19 cells.

(K) Quantification of ciliary length in WT or *Marcks* knockdown ARPE-19 cells. In (J–K), at least 100 cilia were quantified for each condition from three replicates. The experiment was performed 3 times with similar results. Data are presented as mean ± SD. Statistics: One-way ANOVA with multiple comparisons (Tukey test). $^{****}p < 0.0001$. See also Figure S5.

(L) Schematic of the role of MARCKS in targeting CDC42 during ciliogenesis and ciliary growth. MARCKS anchors to the ciliary membrane via a myristoylation site, which then recruits CDC42. The ciliary targeted CDC42 is essential for maintaining the vesicle trafficking required for ciliogenesis and ciliary extension. In the absence of MARCKS, cells either fail to form a cilium or exhibit shortened cilia.

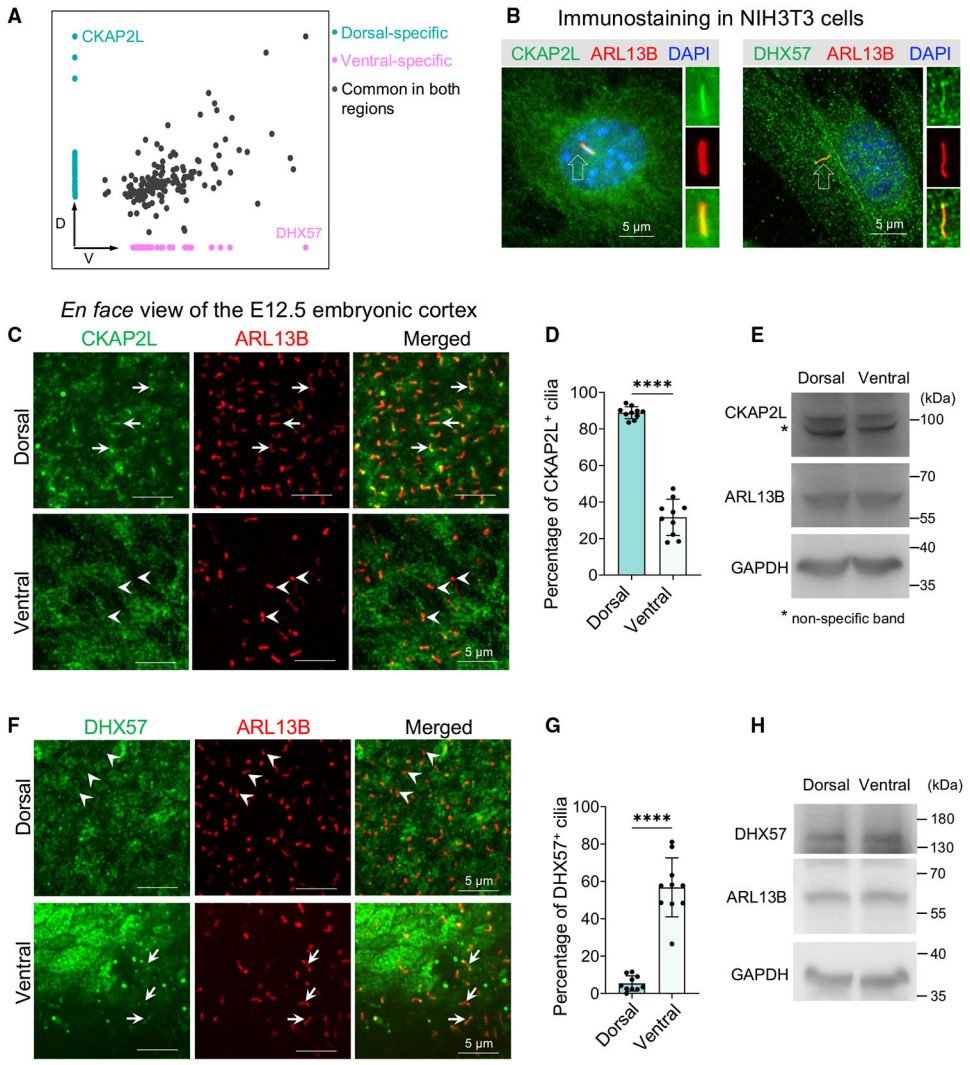

Figure 5. Brain cilium proteomics uncovers region-specific variations in radial glial ciliary composition

(A) Scatterplot of ciliary candidates in dorsal versus ventral regions. The dorsal-specific, ventral-specific, and common ciliary candidates in both regions are listed in Table S4.

(B) Representative images of immunofluorescence staining showing that CKAP2L and DHX57 are present in the primary cilia of NIH3T3 cells. The cilium pointed by the white arrow is magnified and displayed on the right side.

(C) *En face* views of whole-mount WT embryonic mouse brain following immunofluorescence staining with an anti-CKAP2L antibody. White arrows indicate representative cilia positive for CKAP2L in the dorsal region; white arrowheads denote cilia lacking CKAP2L immunoreactivity in the ventral region.

(D) Quantification of CKAP2L-positive cilia in (C). $n = 10$ areas in each region from three mice were quantified and pooled.

(E) Western blotting results of CKAP2L expression levels in the dorsal and ventral regions of E12.5 mouse telencephalon.

(F) *En face* views of whole-mount embryonic WT mouse brain following immunofluorescence staining with an anti-DHX57 antibody. White arrows indicate representative cilia positive for DHX57 in the ventral region; white arrowheads denote cilia lacking DHX57 immunoreactivity in the dorsal region.
(G) Quantification of DHX57-positive cilia in (F). $n = 10$ areas in each region from three mice were quantified and pooled.
(H) Western blotting results of DHX57 expression levels in the dorsal and ventral brain regions of E12.5 mouse.
Data in (D) and (G) are presented as mean ± SD. Statistics: two-tailed Student's *t* test. ****$p < 0.0001$. Scale bars, 5 μm.

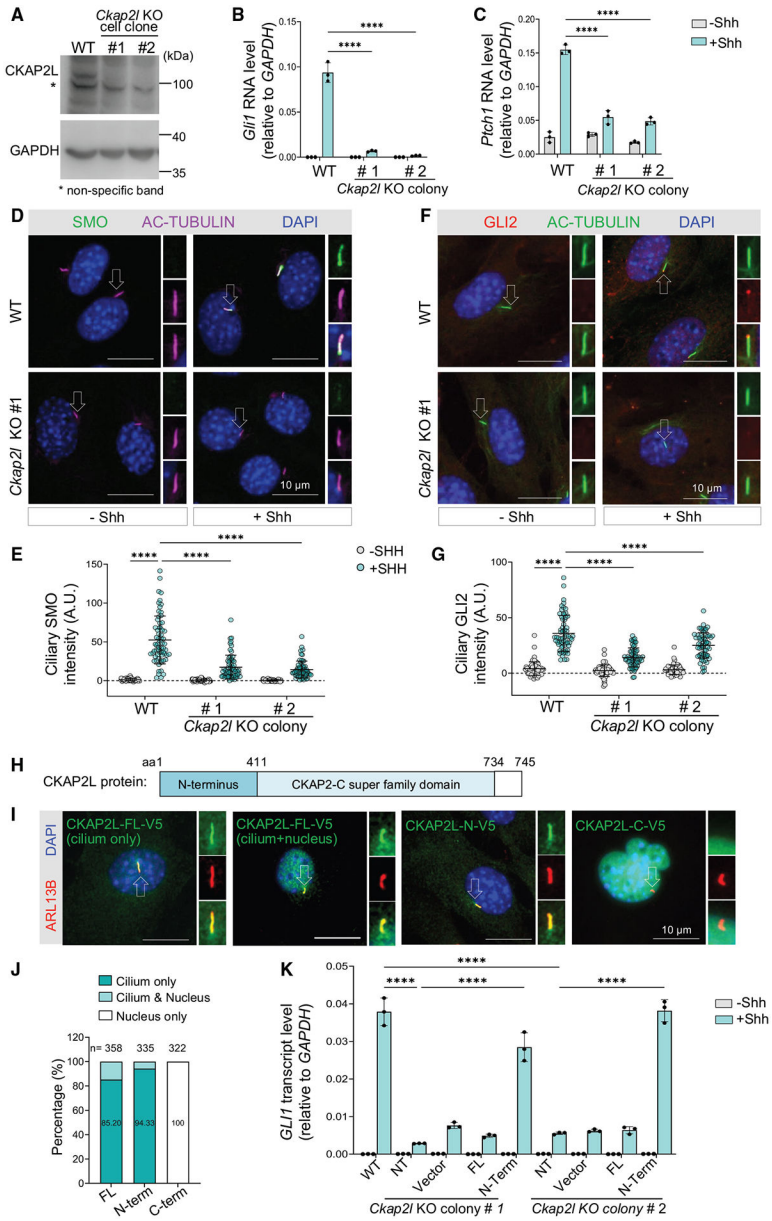

Figure 6. CKAP2L regulates cilium-dependent cell signaling

(A) Western blot analysis showing the absence of CKAP2L protein in the *Ckap2l* CRISPR/Cas9 knockout NIH3T3 cell clones. Asterisk indicates a non-specific band.

(B and C) Hh signaling levels in WT or *Ckap2l* KO NIH3T3 cells were assessed by the transcript levels of the Hh-target genes, *Gli1* and *Ptch1*, via qPCR. $n = 3$ technical replicates; experiments were performed 3 times with similar results. Data are shown as mean ± SD. Statistics: two-way ANOVA with multiple comparisons (Tukey test), ****$p < 0.0001$.

(D) Immunofluorescence of SMO in the cilia in WT and *Ckap2l* KO NIH3T3 cells. Cells were treated with vehicle or Shh for 24 h before being fixed for staining. The cilium pointed by the white arrow is magnified and displayed on the right side.

(E) Quantification of SMO fluorescence intensity in the cilium. For each experimental condition, 62–65 cilia were quantified from three replicates. A.U., arbitrary unit. Data are

shown as mean ± SD. Statistics: two-way ANOVA with multiple comparisons (Tukey test), ****$p < 0.0001$.

(F) Immunofluorescence staining of endogenous GLI2 in the cilia of WT or *Ckap2l* KO NIH3T3 cells. Cells were treated with vehicle or Shh for 24 h before being fixed for staining. The cilium pointed by the white arrow is magnified and displayed on the right side.

(G) Quantification of GLI2 fluorescence intensity at the cilium tips. For each experimental condition, 62–65 cilia were quantified from three replicates. A.U., arbitrary unit. Data are shown as mean ± SD. Statistics: two-way ANOVA with multiple comparisons (Tukey test), ****$p < 0.0001$.

(H) Diagram showing the CKAP2L protein structure.

(I) Representative images showing localization of CKAP2L full length (FL), N- and C terminus in NIH3T3 cells.

(J) Percentage of cells expressing the indicated construct localized to the cilium or nucleus.

(K) Hh signaling levels in WT cells and *Ckap2l* KO NIH3T3 cells that express full-length CKAP2L, N-terminal form, or the blank vector. Hh activity was assessed by *GLI1* transcript levels. $n = 3$ technical replicates. Experiments were performed 3 times with similar results. Data are shown as mean ± SD. Statistics: two-way ANOVA with multiple comparisons (Tukey test), ****$p < 0.0001$. Scale bars, 10 μm.

See also Figure S6.

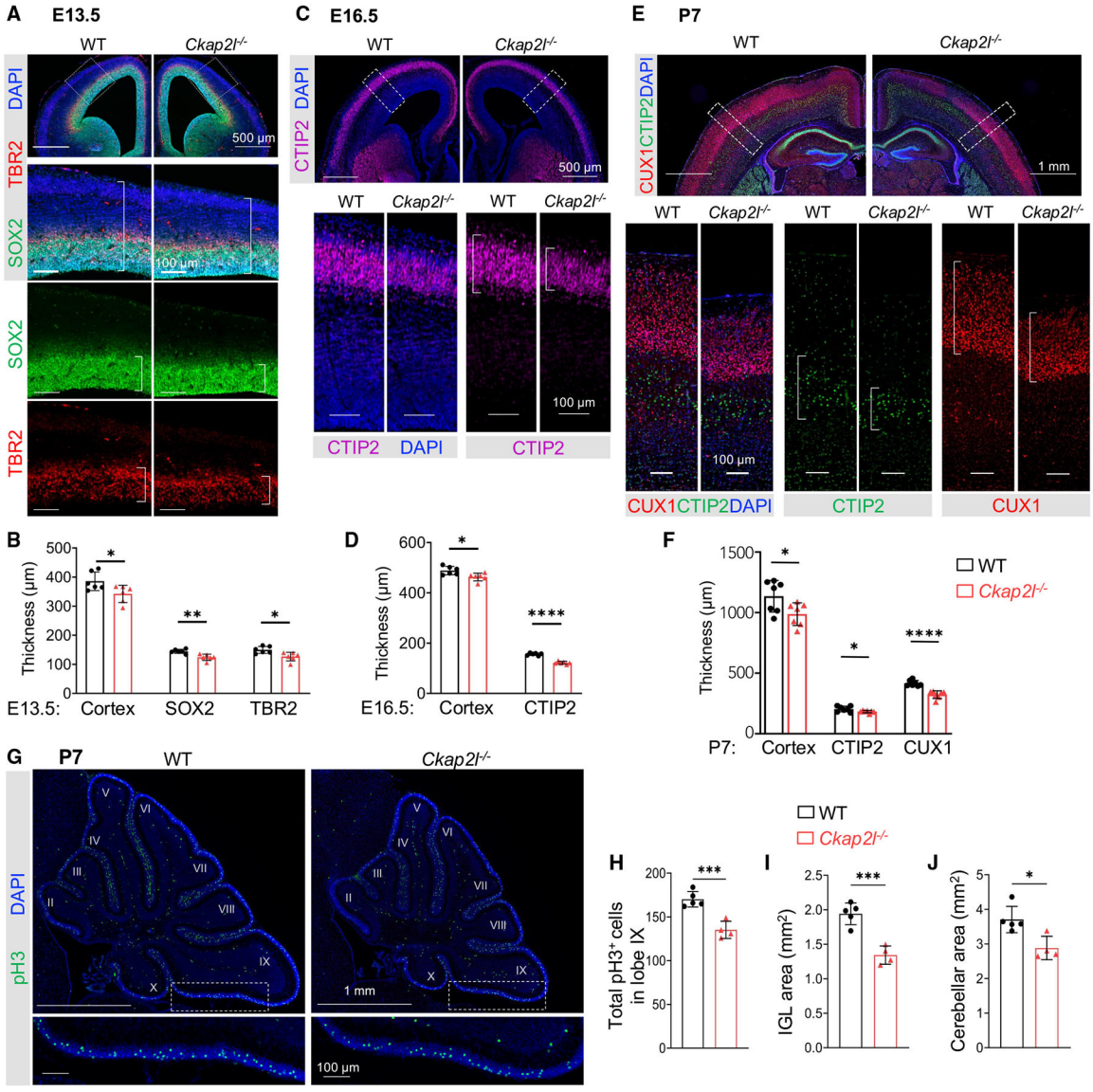

Figure 7. *CKAP2L*$^{-/-}$ mouse exhibits reduced neurogenesis

(A) Representative images of E13.5 brain sections stained with SOX2 and TBR2. Areas in white dashed boxes are magnified and displayed at the bottom. White brackets demarcate the thickness of the indicated layer. Scale bars, 500 μm (top) and 100 μm (bottom).

(B) Quantification of the thickness of the indicated layers in (A). Coronal sections at the same rostral-caudal level indicated in (A) were used for quantification.

(C) Representative images of E16.5 brain sections stained with CTIP2. Areas in white dashed boxes are magnified and displayed at the bottom. Scale bars, 500 μm (top) and 100 μm (bottom).

(D) Quantification of the thickness of the indicated layers in (C). Coronal sections at the same rostral-caudal level indicated in (C) were used for quantification.

(E) Representative images of P7 brain sections stained with CTIP2 and CUX1. Areas in white dashed boxes are magnified and displayed at the bottom. Scale bars, 1 mm (top) and 100 μm (bottom).

(F) Quantification of the thickness of the indicated layers in (E). Coronal sections at the same rostral-caudal level indicated in (E) were used for quantification. For (B), (D), and (F), $n = 6–7$ brains were quantified for each genotype. Data are presented as mean ± SD. Statistics: two-tailed Student's *t* test. ****$p < 0.0001$; **$p < 0.01$; *$p < 0.05$.

(G) Sagittal sections of cerebellum at the same medio-lateral levels from P7 WT and *Ckap2l*$^{-/-}$ mice. Sections were immuno-stained with anti-pH3 antibody. White dashed boxes are magnified and displayed at the bottom. Lobes are indicated by Roman numbers. Scale bars, 1 mm (top) and 100 μm (bottom).

(H) Quantification of the number of pH3-positive cells in the EGL in lobe IX in the sections of the same medio-lateral levels.

(I and J) Quantification of the IGL area and cerebellar area in P7 mice measured at the same medio-lateral level.

For (H–J), $n = 4$ or 5 cerebella were quantified for each genotype. Data are presented as mean ± SD. Statistics: two-tailed Student's *t* test. ***$p < 0.001$; *$p < 0.05$.

See also Figures S7, S8, S9, and S10.

KEY RESOURCES TABLE

REAGENT or RESOURCE	SOURCE	IDENTIFIER
Antibodies		
Mouse anti-ARL13B (1:1000 for IF)	NeuroMab	Cat#: N295B/66 RRID: AB_2895580
Rabbit anti-ARL13B (1:500 for IF, 1:2000 for WB)	Proteintech	Cat#: 17711-1-AP RRID: AB_2060867
Rat anti-ARL13B (1:200 for IF)	BiCell Scientific	Cat#: 90413 RRID: AB_3170226
Rabbit anti-SMO (1:500 for IF)	Matthew Scott lab, Stanford University	https://doi.org/10.1126/science.1139740
Mouse anti-acetylated tubulin (1:1000 for IF)	Sigma	Cat#: T6793 RRID: AB_477585
Chicken anti-GFP (1:500 for IF)	Aves labs	Cat#: GFP-1020 RRID: AB_10000240
Rabbit anti-GFP (1:200 for IF)	Thermo Fisher Scientific	Cat#: A-11122 RRID: AB_221569
Goat anti-GLI2 (1:200 for IF)	R&D Systems	Cat#: AF3635 RRID: AB_2111902
Rabbit anti-GLI3 (1:1000 for WB)	Novus Biologicals	Cat#: NBP2-16665 RRID: AB_3263717
Goat anti-GLI3 (1:1000 for WB)	R&D Systems	Cat#: AF3690 RRID: AB_2232499
Mouse anti-V5 (1:500 for IF)	Thermo Fisher Scientific	Cat#: R960-25 RRID: AB_2556564
Rabbit anti-V5 (1:500 for IF, 1:2000 for WB)	Cell Signaling Technology	Cat#: 13202S RRID: AB_2687461
Mouse anti-γ-tubulin (1:500 for IF)	Proteintech	Cat#: 66320-1-Ig RRID: AB_2857350
Mouse anti-γ-tubulin (1:200 for IF)	Sigma	Cat#: T6557 RRID: AB_477584
Mouse anti-GAPDH (1:2000 for WB)	Santa Cruz Biotechnology	Cat#: sc-32233 RRID: AB_627679
Goat anti-SOX2 (1:500 for IF)	R&D Systems	Cat#: AF2018-SP RRID: AB_355110
Rabbit anti-TBR2 (1:500 for IF)	Abcam	Cat#: ab23345 RRID: AB_778267
Mouse anti-NeuN (1:200 for IF)	Sigma	Cat#: MAB377 RRID: AB_2298772
Mouse anti-NeuN (1:500 for IF)	Abcam	Cat#: ab104224 RRID: AB_10711040
Rabbit anti-CTIP2 (1:200 for IF)	Abcam	Cat#: ab28448 RRID: AB_1140055
Rat anti-CTIP2 (1:500 for IF)	Abcam	Cat#: ab18465 RRID: AB_2064130
Rabbit anti-CUX1 (1:200 for IF)	Proteintech	Cat#: 11733-1-AP RRID: AB_2086995
Rabbit anti-pH3 (1:500 for IF)	Cell Signaling Technology	Cat#: 9701S RRID: AB_331535
Rabbit anti-RPS3 (1:100 for IF)	Proteintech	Cat#: 11990-1-AP RRID: AB_2180758
Rabbit anti-RPL4 (1:100 for IF)	Proteintech	Cat#: 11302-1-AP RRID: AB_2181909
Rabbit anti-RPL10A (1:100 for IF)	Proteintech	Cat#: 16681-1-AP RRID: AB_2181281
Rabbit anti-RPL11 (1:100 for IF)	Proteintech	Cat#: 16277-1-AP RRID: AB_2181292
Mouse anti-RPL19 (1:100 for IF)	Santa Cruz Biotechnology	Cat#: sc-100830 RRID: AB_2181588
Rabbit anti-RPL19 (1:100 for IF)	Proteintech	Cat#: 14701-1-AP RRID: AB_2181587
Mouse anti-RPS23 (1:100 for IF)	Santa Cruz Biotechnology	Cat#: sc-100837 RRID: AB_2180354
Rabbit anti-RPL23A (1:100 for IF)	Proteintech	Cat#: 16386-1-AP RRID: AB_2269755
Mouse anti-EIF3C (1:100 for IF)	Santa Cruz Biotechnology	Cat#: sc-74507 RRID: AB_1122487
Rabbit anti-EIF3C (1:100 for IF)	Proteintech	Cat#: 12733-1-AP RRID: AB_2096747
Mouse anti-EEF1G (1:100 for IF)	Proteintech	Cat#: 68148-1-Ig RRID: AB_2923672
Rabbit anti-EEF2 (1:100 for IF)	Proteintech	Cat#: 20107-1-AP RRID: AB_10950401
Mouse anti-EIF4A2 (1:100 for IF)	Santa Cruz Biotechnology	Cat#: sc-137148 RRID: AB_2097384
Rabbit anti-EIF4A2 (1:100 for IF)	Proteintech	Cat#: 11280-1-AP RRID: AB_2097378
Rabbit anti-MARCKS (1:100 for IF)	Proteintech	Cat#: 20661-1-AP RRID: AB_2878719
Rabbit anti-MARCKS (1:200 for IF, 1:1000 for WB)	Proteintech	Cat#: 10004-2-Ig RRID: AB_2140311

REAGENT or RESOURCE	SOURCE	IDENTIFIER
Mouse anti-MARCKS (1:100 for IF, 1:500 for WB)	Santa Cruz Biotechnology	Cat#: sc-100777 RRID: AB_1125958
Mouse anti-CDC42 (1:100 for IF)	Santa Cruz Biotechnology	Cat#: sc-8401 RRID: AB_627233
Rabbit anti-mouse CKAP2L (1:200 for IF, 1:2000 for WB)	Dr. Shin-ichi Sakakibara, Waseda University	https://doi.org/10.1371/journal.pone.0079895
Rabbit anti-human CKAP2L (1:200 for IF)	Proteintech	Cat#: 17143-1-AP RRID: AB_2080720
Rabbit anti-mouse CKAP2 (1:200 for IF)	LifeSpan BioSciences	Cat#: LS-C663998-200
Mouse anti-human CKAP2 (1:200 for IF)	Sigma	Cat#: SAB1402567 RRID: AB_10637333
Rabbit anti-DHX57 (1:200 for IF, 1:1000 for WB)	Proteintech	Cat#: 24525-1-AP RRID: AB_2879590
Alexa Fluor 647 Streptavidin	Jackson ImmunoResearch Labs	Cat#: 016-600-084 RRID: AB_2341101
Donkey anti-Mouse Alexa Fluor 488	Jackson ImmunoResearch Labs	Cat#: 715-545-151 RRID: AB_2341099
Donkey anti-Mouse Rhodamine	Jackson ImmunoResearch Labs	Cat#: 715-025-151 RRID: AB_2340767
Donkey anti-Mouse Alexa Fluor 647	Jackson ImmunoResearch Labs	Cat#: 715-605-151 RRID: AB_2340863
Donkey anti-Rabbit Alexa Fluor 488	Jackson ImmunoResearch Labs	Cat#: 711-545-152 RRID: AB_2313584
Donkey anti-Rabbit Rhodamine	Jackson ImmunoResearch Labs	Cat#: 711-025-152 RRID: AB_2340588
Donkey anti-Rabbit AlexaFluror 647	Jackson ImmunoResearch Labs	Cat#: 711-605-152 RRID: AB_2492288
Donkey anti- Rat Alexa Fluor 488	Jackson ImmunoResearch Labs	Cat#: 712-545-153 RRID: AB_2340684
Donkey anti- Rat Rhodamine	Jackson ImmunoResearch Labs	Cat#: 712-025-153 RRID: AB_2340636
Donkey anti- Rat AlexaFluror 647	Jackson ImmunoResearch Labs	Cat#: 712-605-153 RRID: AB_2340694
Donkey anti-Chicken Alexa Fluor 488	Jackson ImmunoResearch Labs	Cat#: 703-545-155 RRID: AB_2340375
Donkey anti-Goat Alexa Fluor 488	Jackson ImmunoResearch Labs	Cat#: 705-545-147 RRID: AB_2336933
Donkey anti-Goat 594	Jackson ImmunoResearch Labs	Cat#: 705-585-147 RRID: AB_2340433
HRP-Conjugated Donkey anti-Mouse IgG	Jackson ImmunoResearch Labs	Cat#: 715-035-151 RRID: AB_2340771
HRP-Conjugated Donkey anti-Rabbit IgG	Jackson ImmunoResearch Labs	Cat#: 711-035-152 RRID: AB_10015282
HRP-Conjugated Goat anti-Rabbit IgG	Cell Signaling Technology	Cat#: 7074S RRID: AB_2099233
HRP-Conjugated Neutravidin	Thermo Fisher Scientific	Cat#: A2664
HRP-Conjugated Streptavidin	Thermo Fisher Scientific	Cat#: N100
Bacterial strains		
TOP10	Thermo Fisher Scientific	Cat#: C404010
Stbl3	Thermo Fisher Scientific	Cat#: C737303
Biological samples		
Cilium-TurboID transgenic mouse brains	This paper	N/A
CKAP2L$^{-/-}$ mouse cerebella and brains	This paper	N/A
Chemicals, peptides, and recombinant proteins		
Biotin	Sigma	Cat#: B4501
Protease Inhibitor Cocktail	Sigma	Cat#: 11836170001
Recombinant mouse Shh,N terminus	R&D Systems	Cat#: 461-SH-025
bFGF	Sigma	Cat#: GF44610UG
DMEM medium	Fisher Scientific	Cat#: MT10013CM
DMEM/F12 medium	Fisher Scientific	Cat#: 11-320-033
Neurobasal medium	Thermo Fisher Scientific	Cat#: 21103-049
N-2 supplement	Thermo Fisher Scientific	Cat#: 17502001
GlutaMAX supplement	Thermo Fisher Scientific	Cat#: 35-050-061

REAGENT or RESOURCE	SOURCE	IDENTIFIER
Penicillin-Streptomycin	Thermo Fisher Scientific	Cat#: 15140122
Neutravidin agarose resin	Thermo Fisher Scientific	Cat#: 29201
Streptavidin magnetic beads	Thermo Fisher Scientific	Cat#: 88817
Lipofectamine 2000	Thermo Fisher Scientific	Cat#: 11668019
CalPhos Transfection kit	Thermo Fisher Scientific	Cat#: NC9567834
Mm00494645_m1 (*GLI1*) Taqman probe	Thermo Fisher Scientific	Cat#: 4331182
Mm00436026_m1 (*PTCH1*) Taqman probe	Thermo Fisher Scientific	Cat#: 4331182
Mm99999915_g1 (*GAPDH*) Taqman probe	Thermo Fisher Scientific	Cat#: 4331182
Mm01210070_g1 (*CKAP2*) Taqman probe	Thermo Fisher Scientific	Cat#: 4331182
Hs05030235_g1 (*MARCKS*) Taqman probe	Thermo Fisher Scientific	Cat#: 4331182
Hs02786624_g1 (*DAPDH*) Taqman probe	Thermo Fisher Scientific	Cat#: 4331182
Fluoromount-G	SouthernBiotech	Cat#: 0100-01
O.C.T. compound	Fisher Scientific	Cat#: 23-730-571
DAPI	Thermo Fisher Scientific	Cat#: D21490
Hoechst 33342	Thermo Fisher Scientific	Cat#: 62249
Chemiluminescence substrates	Thermo Fisher Scientific	Cat#: 34577
Pierce Silver Stain Kit	Thermo Fisher Scientific	Cat#: 24612
Ribonucleoside vanadyl complex	New England Biolabs	Cat#: S1402S
Proteinase K	Fisher Scientific	Cat#: 25530049
Proteinase K	New England Biolabs	Cat#: P8107S
RNase A	Fisher Scientific	Cat#: 12091021
Endogenous Biotin-Blocking Kit	Fisher Scientific	Cat#: E–21390
SSC buffer	Fisher Scientific	Cat#: 15557044
Alexa Fluor 488 Tyramide SuperBoost Kit	Fisher Scientific	Cat#: B40932
Acryloyl-X SE	Thermo Fisher Scientific	Cat#: A20770
qScript XLT One-Step RT-qPCR ToughMix, Low ROX	QuantaBio	Cat#: 76047-136
PerfeCTa SYBR Green FastMix Low ROX	QuantaBio	Cat#: 95074-250
Pierce TCEP HCl	Thermo Scientific	Cat#: 20490
2-Chloroacetamide ≥98%	Sigma-Aldrich	Cat#: 22790
Trypsin	Promega	Cat#: V5111
Calcium chloride	Sigma-Aldrich	Cat#: C5670
Resin, Acquity UPLC® BEH 1.7 μm C18	Waters	Cat#: 186004690
Water (Optima LC-MS grade)	Fisher Scientific	Cat#: W6-4
Acetonitrile	Honeywell	Cat#: AH015-4
Methanol	J.T. Baker	Cat#: 9093-33
Chloroform	Fisher Scientific	Cat#: C298-4
Formic acid 90%	J.T.Baker	Cat#: 0129-01
TFA	Sigma-Aldrich	Cat#: T6508-10AMP
Polymicro fused silica capillary tubing 100 μm	Molex	Cat#: 1068150023
11 PP Vial Crimp/Snap 250 μL	Thermo Scientific	Cat#: C4011-13
Snap-it Seal	Thermo Scientific	Cat#: C4011-53
Protein LoBind Tube 1.5 mL	Eppendorf	Cat#: 022431081

REAGENT or RESOURCE	SOURCE	IDENTIFIER
Protein LoBind Tube 2.0 mL	Eppendorf	Cat#: 022431102
Pierce HeLa protein digest standard	Thermo Scientific	Cat#: 88329
Urea	Sigma-Aldrich	Cat#: U5128-110G
1 M TEAB	Thermo Scientific	Cat#: 90114
TMT 10-plex	Thermo Scientific	Cat#: 90110 (Lot#: WI319139)
50% Hydroxylamine	Thermo Scientific	Cat#: 90115
Pierce High pH RP peptide fractionation kit	Thermo Scientific	Cat#: 84868
Experimental models: Cell lines		
NIH3T3cells	ATCC	Cat#: CRL-1658
HEK293T cell	ATCC	Cat#: CRL-3216
SH-SY5Y cells	ATCC	Cat#: CRL-2266
ARPE-19 cells	ATCC	Cat#: CRL-2302
293 EcR-Shh-N cell line	Rajat Rohatgi lab, Stanford University	https://doi.org/10.1083/jcb.200907126
Marcks CRISPR/Cas9 knockout NIH3T3cells	This paper	N/A
Ckap2l CRISPR/Cas9 knockout NIH3T3cells	This paper	N/A
Ckap2l CRISPR/Cas9 knockout MEF cells	This paper	N/A
Experimental models: Organisms/strains		
Cilium-TurboID transgenic mouse	This paper	N/A
Ckap2l$^{-/-}$ mouse	This paper	N/A
Oligonucleotides		
Marcks sgRNA-1	5'AGGGAGAAGCCACCGCCGAG3'	N/A
Marcks sgRNA-2	5'ATTTGCTTTGGAAGGCGACG3'	N/A
Ckap2l sgRNA-1	5'GTCGCCGTAGAGCCATGGTG3'	N/A
Ckap2l sgRNA-2	5'CCGCGGCTGCGCTGGCAGTG3'	N/A
Genotyping for Ckap2l$^{-/-}$ mice (Forward)	5'AGGAAGCTTCTTTACAAGGCAGT3'	N/A
Genotyping for Ckap2l$^{-/-}$ mice (Reverse-1)	5'TCTGGCTACCAAAATTACTCAGAGG3'	N/A
Genotyping for Ckap2l$^{-/-}$ mice (Reverse-2)	5'GGGGCAGATATTCTTGGCTTTTAG3'	N/A
Genotyping for Cilia-TurboID mice (GAPDH-Forward)	5'AGCCATCAGCTATGCACGTA3'	N/A
Genotyping for Cilia-TurboID mice (GAPDH-Reverse)	5'GCCTCGGCTGCTCAAAGAAT3'	N/A
Genotyping for Cilia-TurboID mice (Transgene-Forward)	5'GAATCGGCGAGCTGAAGAGT3'	N/A
Genotyping for Cilia-TurboID mice (Transgene-Reverse)	5'CATTGGGCCATTTGACTCGC3'	N/A
Recombinant DNA		
pFUGW-MARCKS-YFP	This paper	N/A
pFUGW-MARCKS-Myri-Mut-YFP	This paper	N/A
pFUGW-MARCKS-Phos-Mut-YFP	This paper	N/A

REAGENT or RESOURCE	SOURCE	IDENTIFIER
pFUGW-CKAP2L-GFP	This paper	N/A
pFUGW-CKAP2L-V5	This paper	N/A
pFUGW-CKAP2L-N-term-V5	This paper	N/A
pFUGW-CKAP2L-C-term-V5	This paper	N/A
pFUGW-CKAP2-YFP	This paper	N/A
shRNA Control	This paper	N/A
Marcks shRNA-1	This paper	N/A
Marck shRNA-2	This paper	N/A
Ckap2 shRNA-1	This paper	N/A
Ckap2 shRNA-2	This paper	N/A
PX330-GFP-Marcks sgNRA-1	This paper	N/A
PX330-GFP-Marcks sgNRA-2	This paper	N/A
PX330-GFP-Ckap2l sgNRA-1	This paper	N/A
PX330-GFP-Ckap2l sgNRA-2	This paper	N/A
Instruments		
Orbitrap Fusion Lumos	Thermo Scientific	N/A
EASY-nLC 1200	Thermo Scientific	Cat#: LC140
Laser-based micropipette puller system	Sutter Instrument	Cat#: P-2000
Pressure bomb	customized with Swagelok	https://www.swagelok.com/
Thermomixer F1.5	Eppendorf	Cat#: 5384000020
Microfuge18 centrifuge	Beckman Coulter	Cat#: 367160
Vacuum Centrifuge	Labconco	Cat#: 7810016
Software and algorithms		
Prism 9 software	GraphPad	https://www.graphpad.com/scientific-software/prism/
LAS X Life Science Microscope software	Leica	https://www.leica-microsystems.com/products/microscope-software/p/leica-las-x-ls/
ImageJ	NIH	https://imagej.nih.gov/ij/
Image Lab	BioRad	http://www.bio-rad.com/ja-jp/product/imagelab-software
OriginLab	OriginLab Corporation	https://www.originlab.com/
ProLuCID	IP2, Bruker Scientific LLC	http://fields.scripps.edu/yates/wp/?page_id=821
DTASelect2.0	IP2, Bruker Scientific LLC	http://fields.scripps.edu/yates/wp/?page_id=816
Census2.0	IP2, Bruker Scientific LLC	http://fields.scripps.edu/yates/wp/?page_id=824
RAWConverter	John R. Yates III, Scripps Research, La Jolla	http://fields.scripps.edu/rawconv/
XCalibur	Thermo Scientific	Cat#: OPTON-30965-7